Unconventional Magnetism, Sliding Ferroelectricity, and Magneto-Optical Kerr Effects in a Multiferroic Bilayer

Xinfeng Chen,[†] Ning Ding,[‡] Paolo Barone,[¶] Carlo Rizza,[§] Shuai Dong,[‡] Wei Ren,[‖] Paolo G. Radaelli,[*,⊥] Gaoyang Gou,[*,†] and Alessandro Stroppa[*,#]

[†]*Frontier Institute of Science and Technology, State Key Laboratory of Electrical Insulation and Power Equipment, Xi'an Jiaotong University, Xi'an 710049, China.*

[‡]*School of Physics, Southeast University, Nanjing 211189, China.*

[¶]*CNR-SPIN, Area della Ricerca di Tor Vergata, Via del Fosso del Cavaliere 100, I-00133 Rome, Italy.*

[§]*Department of Physical and Chemical Sciences, University of L'Aquila, Via Vetoio I-67100 Coppito, L'Aquila, Italy.*

[‖]*Physics Department, Shanghai Key Laboratory of High Temperature Superconductors, State Key Laboratory of Advanced Special Steel, International Centre of Quantum and Molecular Structures, Shanghai University, Shanghai 200444, China.*

[⊥]*Clarendon Laboratory, Department of Physics, University of Oxford, Oxford OX1 3PU, United Kingdom.*

[#]*CNR-SPIN, c/o Department of Physical and Chemical Sciences, University of L'Aquila, Via Vetoio I-67100 Coppito, L'Aquila, Italy.*

E-mail: paolo.radaelli@physics.ox.ac.uk; gougaoyang@mail.xjtu.edu.cn; alessandro.stroppa@spin.cnr.it

Abstract

Antiferromagnetic (AFM) materials provide a platform to couple altermagnetic (AM) spin-splitting to the magneto-optical Kerr effect (MOKE), with potential for next-generation quantum technologies. In this work, first-principles calculations, symmetry analysis, and $\boldsymbol{k}\cdot\boldsymbol{p}$ modeling are employed to show that interlayer sliding in AFM multiferroic bilayers enables control of electronic, magnetic, and magneto-optical properties. This study reveals an intriguing dimension-driven AM crossover: the 2D paraelectric (PE) bilayer exhibits spin-degenerate bands protected by the $[\mathcal{C}_2\|\mathcal{M}_c]$ spin-space symmetry, whereas the 3D counterpart manifests AM spin-splitting along $k_z \neq 0$ paths. Furthermore, interlayer sliding breaks the $\mathcal{M}_c$ symmetry and stabilizes a ferroelectric (FE) state with compensated ferrimagnetism, where the Zeeman-like field is responsible for the non-relativistic spin-splitting. In the FE phase, spin-orbit coupling (SOC) lifts accidental degeneracies and produces "alternating" spin-polarized bands through the interplay of Zeeman and Rashba effects. Crucially, spin polarization, ferro-valley polarization (ΔE_V), and the Kerr angle (θ_k) can all be reversed by switching either sliding ferroelectricity or Néel vector. Our findings reveal the rich coupling among electronic, magnetic, and optical orders in sliding multiferroics, illustrating the new prospects for ultra-low-power spintronic and optoelectronic devices.

Keywords: altermagnetism, compensated ferrimagnetism, sliding ferroelectricity, magneto-optical Kerr effect, ferro-valley, multiferroics

INTRODUCTION

Altermagnets (AMs) are compensated magnets in which, similar to ferromagnetic (FM) materials, Kramers spin-degeneracy is lifted in such a way as to allow $\vec{k}/-\vec{k}$ symmetric spin-split energy bands in certain regions of the Brillouin zone.[1–3] AMs are a subset of compensated magnets (historically called antiferromagnets, AFMs) characterized by two symmetry-related collinear but opposite spin-sublattices. In order to allow non-relativistic spin-splitting, the

two spin-sublattices must not be related by either a translation ($\vec{t}$, leading to time-reversal $\mathcal{T}$ symmetry) or inversion ($\mathcal{I}$, leading to $\mathcal{TI}$ symmetry). Instead, opposite spin-sublattices in AMs are connected by real-space rotation ($\mathcal{R}$) or mirror ($\mathcal{M}$) operations.[3,4] Unlike the case of $\mathcal{T}$ and $\mathcal{TI}$ symmetries, this relation does not always lead to exact symmetries of the magnetically ordered phase. The exact or approximate $[\mathcal{C}_2\|\mathcal{R}]$ (in spin group framework[5,6]) or $\mathcal{TR}$ (in Shubnikov framework[7]) symmetries are hallmarks of AMs and offer a basis for their classification. Since their recognition as a distinct class, AMs have been intensively studied to confirm their distinctive electronic structures. Initial reports focused on RuO_2[8] (with later debate about its magnetism[9]), CrSb[10] and Mn_5Si_3.[11] Moreover, several reports made a connection between AMs and non-collinear magnets such as $MnTe_2$, which were known to support spin-splitting that are very similar to those of AMs.[1] By combining FM-like and AFM-like magnetic properties in a single phase, AMs exhibit unique physical characteristics and offer application advantages beyond those of other magnetic materials.[12,13]

An important strand of this research focused on the role of SOC. In the absence of SOC, AMs support spin-splitting of non-relativistic origin that can be as large as 1 eV, the resulting band structure being insensitive to the direction of the Néel vector. When SOC is introduced, additional band structure modifications and momentum-space splitting take place, which depend on the direction of the magnetic moment and are generally associated with the emergence of a small degree of spin non-collinearity. This phenomenon was observed in MnTe[14] and is sometimes called 'weak' altermagnetism, in analogy to the well-known effect leading to 'weak ferromagnetism'. When SOC-dependent weak effects are taken into account, they may lead to further classifications of AMs, such as the one recently proposed by S.-W. Cheong.[15] In general, spin-splitting associated with both 'strong' and 'weak' altermagnetism can lead to unique properties, such as spin current and spin torque generation,[16,17] the crystal hall effect,[18] giant tunneling magnetoresistance[16,19] and chiral magnons,[20,21] thus attracting great attention in the fields of spintronics, magnetic storage, dissipationless magneto-electrics and quantum computing.[6,22,23]

The magneto-optical Kerr effect (MOKE) is the rotation of linearly polarized light upon reflection from magnetic materials; the rotation angle is termed Kerr angle, θ_k. This effect provides a way to probe magnetic ordering and investigate key magnetic properties.[24] Initially, MOKE was observed exclusively in FM and ferrimagnetic (FiM) materials with non-zero magnetization.[25] More recently, MOKE was observed in nearly compensated non-collinear AFMs,[26] and also in collinear AM candidates such as RuO_2 and $CoNb_3S_6$,[27] where θ_k reverses with crystal handedness. Time-resolved MOKE measurements have been further demonstrated to be effective for ultrafast tracking of spin dynamics in epitaxial MnTe films.[2] Combined with angle-resolved photoemission spectroscopy (ARPES),[28] MOKE provides a versatile and experimentally accessible probe for unambiguous detection of AM.

For a non-zero Kerr angle to be allowed, a necessary condition is that $\mathcal{T}$ and $\mathcal{TI}$ symmetries be simultaneously broken,[29,30] as is the case for AMs. However, a second necessary condition is that FM ordering should be allowed. Therefore, only a subset of AMs is MOKE-active.[15,31] Moreover, the MOKE arises only via SOC, because FM moments (even weak ones) are forbidden by AM spin group symmetries. Consequently, FE polarization coupled to spins through SOC can lead to additional multifunctional responses.[22] In some cases, FE polarization can lead to a transition from non-AM and MOKE-inactive to MOKE-active AM.[32–34] For example, the centrosymmetric $MnPSe_3$ monolayer displays collinear AFM magnetic ordering, where spin-degeneracy is protected by $\mathcal{TI}$ symmetry. By introducing out-of-plane polarization, via either an applied vertical electric field or Janus structure formation (substituting Se with S in one atomic layer),[35] the $\mathcal{TI}$ symmetry is broken, and a mirror symmetry relates the magnetic moments of two oppositely oriented Mn spin-sublattices. This transformation converts the centrosymmetric AFM monolayer into a 2D polar AM material, while simultaneously activating the MOKE. Another promising strategy for breaking $\mathcal{I}$ symmetry in 2D materials involves stacking two monolayers in specific interlayer configurations, leading to net out-of-plane ferroelectricity.[36–39] Consequently, FE polarization and magnetic ordering provide additional degrees of freedom for the simultaneous tuning of the electronic

structure and the MOKE response.

In this paper, we perform first-principles calculations and symmetry analysis to investigate the interplay between magnetism, sliding ferroelectricity, and the MOKE in the 2D AFM H′-Co_2CF_2 multiferroic. In the PE phase, the bilayer exhibits spin-degenerate bands without SOC, protected by the mirror symmetry $\mathcal{M}_c$.[22] In contrast, its bulk phase with 3D periodicity displays AM spin-splitting along reciprocal space paths with $k_z \neq 0$. This highlights a dimension-driven AM crossover between 3D bulk and 2D layered forms. In the FE bilayer with out-of-plane sliding ferroelectricity, the emergence of compensated ferrimagnetism lifts spin-degeneracy even in the absence of SOC. Upon inclusion of SOC, the momentum-dependent spin-splitting gives rise to spin polarization changing within each energy band across the Brillouin zone. We refer to this peculiar behavior as "alternating" spin-polarized bands, which arises from the interplay between Rashba and Zeeman effects. In addition, we observe pronounced spin-valley locking with nontrivial spin-texture. Remarkably, the sign of both the "alternating" spin-polarized bands and θ_k can be reversed either by switching the FE polarization or by reversing the Néel vector. These findings demonstrate how the FE and AFM orderings provide versatile degrees of freedom for engineering MOKE in 2D materials.

RESULTS AND DISCUSSION

Crystal structure and magnetic configuration

Co_2CF_2 belongs to the MXene material family, where each monolayer consists of five closely stacked atomic layers: F-Co-C-Co-F. In its stable H′ phase, the H′-Co_2CF_2 monolayer exhibits out-of-plane FM ordering and polar displacements of the Co cations relative to the anionic plane (see **Figure S1**), making it a multiferroic material with both ferromagnetism and out-of-plane ferroelectricity.[40] MXene can be readily prepared as multilayers. Depending on the interlayer stacking sequence, the structural symmetry and material properties of

2D multilayers can differ significantly from their monolayer counterparts (e.g., 2H-MoS_2).[41]

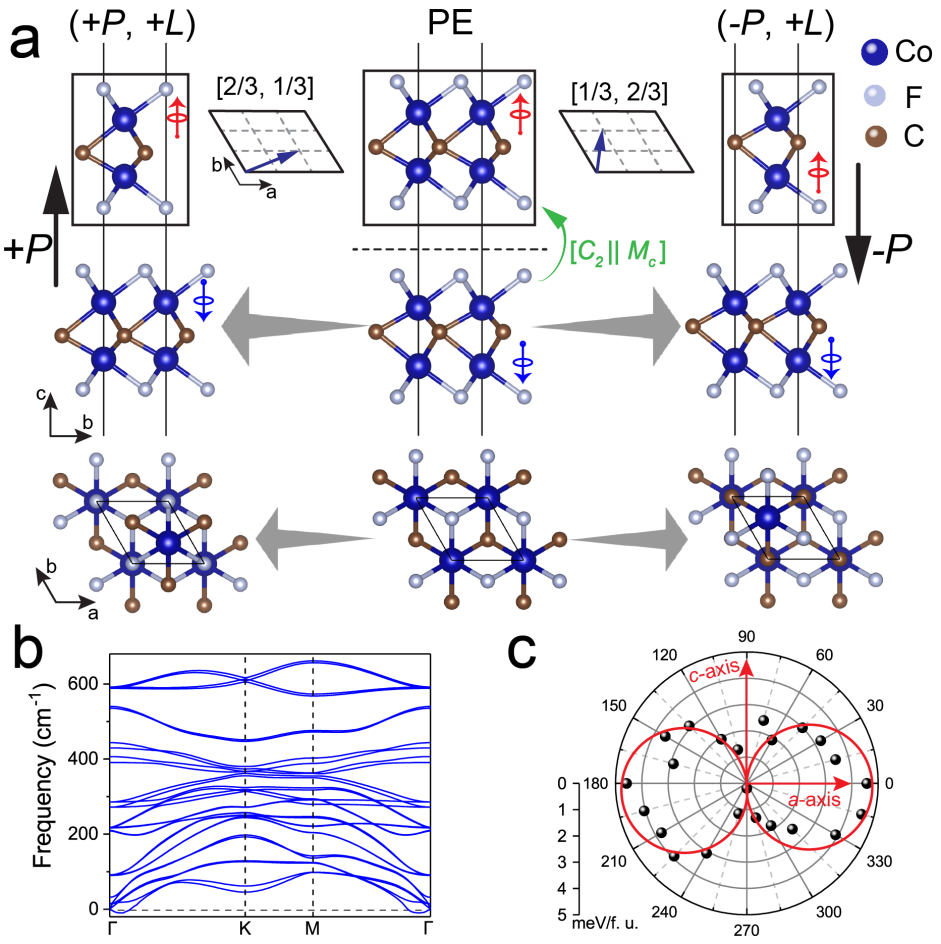

Figure 1: (a) Schematic diagrams of the transition from the PE to FE phase ($\pm P$ states) by the [2/3, 1/3] and [1/3, 2/3] interlayer sliding within H′-Co_2CF_2 bilayer. Both side and top views are shown. The unit cell of H′-Co_2CF_2 monolayer is outlined in black, with Co, C, and F atoms colored in blue, brown, and silver, respectively. Red and blue circled arrows represent the direction of magnetic moments for spin-active Co cations. In the FE phase, out-of-plane polarization direction P is shown by black arrows. (b) Simulated phonon spectrum for the $(+P, +L)$ state of the FE bilayer, indicating no imaginary frequencies and structural instability. (c) Calculated magnetic anisotropy energy (MAE) for the $(+P, +L)$ state, showing the magnetic easy axis along the out-of-plane c-axis after rotating the Néel vector within the ac plane.

The study begins by establishing the reference PE phase for the H′-Co_2CF_2 bilayer. As shown in Figure 1 (a), the PE phase consists of two monolayers with an AA' stacking sequence and antiferroelectric (AFE) configuration. Due to the presence of a mirror plane $\mathcal{M}_c$ between the two monolayers, the corresponding space group is the acentric non-polar

$P\bar{6}m2$. The lowest-energy configuration consists of two antiparallel FM monolayers, yielding a perfectly compensated AFM ordering with type-III magnetic space group (MSG) $P\bar{6}'m'2$ (detailed results are tabulated in **Table S1**). It is important to note that only the Co cations farther from the C atomic layer exhibit non-zero magnetic moments. Here, they are referred to as spin-active Co, labeled with circled arrows in Figure 1 (a). In contrast, the Co cations in the other layer have zero magnetic moments. This coexistence of spin-active and spin-inactive Co cations is the result of differences in orbital occupancy, induced by the varying lengths of Co-C bonds.[40] In the PE phase, two spin-sublattices with opposite Co magnetic moments are connected by the $[\mathcal{C}_2\|\mathcal{M}_c]$ spin-space operation.

However, the PE phase of the bilayer is unstable, as it undergoes a spontaneous PE–FE phase transition induced by the relative sliding of the adjacent layers. As illustrated in Figure 1 (a), after sliding the top monolayer toward the [2/3, 1/3] or [1/3, 2/3] in-plane positions of the bottom monolayer, two stable and equivalent FE structures with AB stacking sequence are formed, corresponding to the acentric polar $P3m1$ space group resulting from the breaking of $\mathcal{M}_c$ reflection. As a result, the Co cations of one monolayer are positioned exactly below or above the F anions of the other monolayer, leading to net interlayer dipoles. Note that the C anions in both monolayers are displaced along the same out-of-plane direction. The estimated polarization is $P = \pm 2.17\ \mu\mathrm{C/cm^2}$ (see **Figure S2** for computational details[42]). As shown in Figure 1 (b), the dynamical stability of the FE bilayer is confirmed by the absence of imaginary frequencies in the phonon band structure.

The lowest-energy configuration is an antiparallel AFM arrangement of the FM monolayers (see **Table S1**). To determine the magnetic easy axis of the FE-AFM bilayer, we evaluate the magnetic anisotropy energy (MAE) by rotating the Néel vector within the ac crystallographic plane. Figure 1 (c) shows an out-of-plane easy axis for the FE-AFM phase. Accordingly, the MSG is $P3m'1$ (**Figure S3**), which also permits ferromagnetism. As the FE-AFM bilayer maintains its insulating character, the net magnetization remains zero by virtue of the Luttinger theorem,[43,44] thus realizing a fully compensated ferrimagnet not en-

forced by symmetry.[45] The resulting multiferroic phase is characterized by the out-of-plane FE polarization P and Néel vector $\mathbf{L} = \mathbf{M}_1 - \mathbf{M}_2$, where the subscripts 1 and 2 correspond to upper and lower monolayers respectively. Within a Landau-theory framework and taking the $P\bar{6}'m'2$ PE phase as the reference structure, four iso-energetic symmetry-equivalent states can be predicted in the H′-Co_2CF_2 multiferroic bilayer, characterized by ($+P$, $+L$), ($+P$, $-L$), ($-P$, $+L$) and ($-P$, $-L$) (see **Figure S4**), mutually related by the broken-symmetry elements $\mathcal{T}$, $\mathcal{M}_c$ and their combination $\mathcal{T}\mathcal{M}_c$. In experiments, the two equivalent FE states can be achieved by applying an external electric field or by optical and mechanical means,[46–48] while the reversal of Néel vector can be accomplished through the current-induced spin-orbit torque method.[49]

Dimension-driven AM crossover in PE phase

Spin-space group (SSG) analysis predicts that the PE bilayer, with $[\mathcal{C}_2\|\mathcal{M}_c]$ spin-space symmetry, should be AM exhibiting non-relativistic spin-splitting at k-points not invariant under $\mathcal{M}_c$.[3,12] However, as depicted in Figure 2 (a), the calculated non-relativistic band structure is completely spin-degenerate. This apparent contradiction can be resolved by noting that all crystalline quasi-momenta of the 2D Brillouin zone are indeed invariant under the $\mathcal{M}_c$ reflection, thus enforcing Kramers-like spin-degeneracy of the full band structure. When out-of-plane translation symmetry is restored, as in a 3D material possessing the same magnetic point group (MPG), the $[\mathcal{C}_2\|\mathcal{M}_c]$ symmetry forces the spin-splitting to be antisymmetric under $k_z \to -k_z$, protecting Kramers-like degeneracy only on the $k_z = 0$ plane.[22] Consistently, Figure 2 (b) demonstrates that AM splitting emerges in the 3D bulk phase (Figure 2 (c)), despite the fact that the 2D and 3D phases have the same MPG. To our knowledge, this is the first example of dimension-driven altermagnetism, with an AM-AFM crossover between 3D and 2D forms despite identical stacking. The dimension-driven altermagnetism deserves further investigations, which are beyond the purpose of the present study.

The spin-degeneracy of non-relativistic bands in the PE-AFM bilayer can be understood as follows. Each FM monolayer displays Zeeman-split bands, which are weakly modified by interactions across the van der Waals gap. The Zeeman-split band structure of the upper monolayer is mirrored in the lower monolayer as a consequence of the $\mathcal{M}_c$ symmetry, showing the same dispersion but with reversed spin polarization due to the opposite effective exchange field. Each overall spin-degenerate band thus displays a hidden Zeeman spin-splitting when projected onto mirror-partner layers, analogously to conventional $\mathcal{TI}$-symmetric AFMs with staggered magnetization on $\mathcal{I}$-related magnetic sublattices.

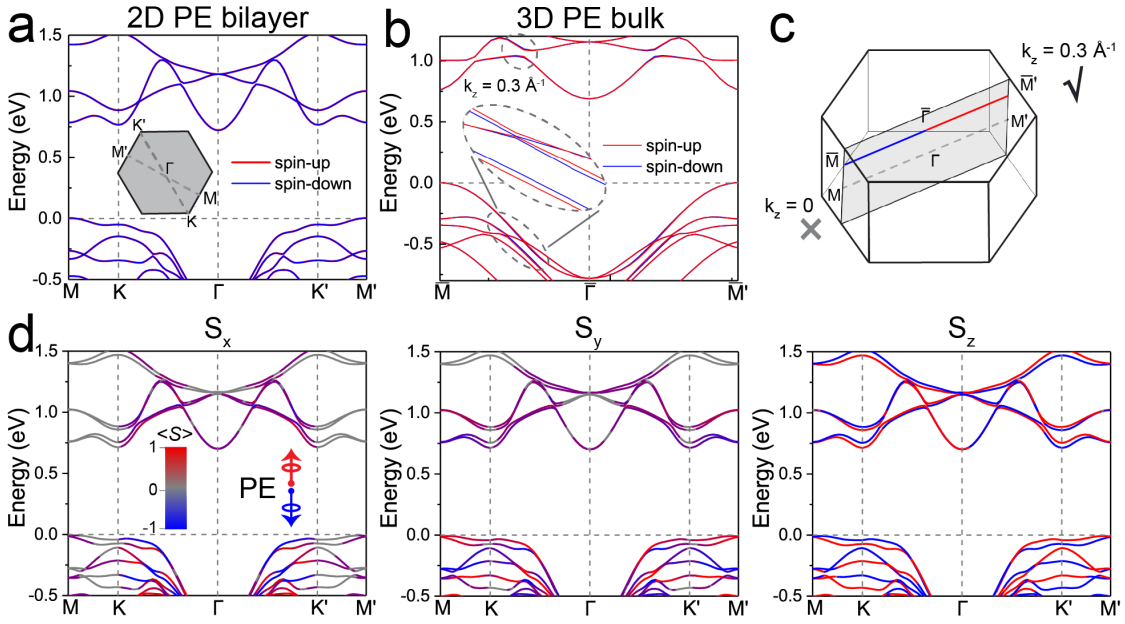

Figure 2: (a) Calculated non-relativistic spin-resolved band structure for the 2D PE phase of the H′-Co_2CF_2 bilayer at $k_z = 0$. The inset shows the high-symmetry reciprocal paths in the 2D Brillouin zone. (b) Calculated non-relativistic spin-resolved band structure for the 3D PE phase of the H′-Co_2CF_2 bulk along the reciprocal path at $k_z = 0.3$ Å^{-1}. (c) Schematic of the 3D Brillouin zone along the $\overline{\text{M}}$–$\overline{\Gamma}$–$\overline{\text{M}'}$ (M–Γ–M′) paths at $k_z = 0.3$ Å^{-1} ($k_z = 0$), showing the corresponding spin split bands. Red and blue colors indicate opposite spin components. Spin-splitting occurs only when $k_z \neq 0$. (d) Relativistic spin-resolved band structure for the 2D PE bilayer with a $+L$ Néel vector. The color bar indicates the expectation values of the spin components from spin-active Co atoms. The Fermi level is set at 0 eV.

As shown in Figure 2 (d), when SOC is included, the $\mathcal{M}_c$ operation is replaced by the antiunitary $\mathcal{TM}_c$ operation, which enforces Kramers-like degeneracy only at the $\mathcal{TM}_c$-invariant Γ and M points, thus allowing SOC-induced spin-splitting in general. In particular,

the double-degeneracy of band edges near the K(K$'$) valleys is lifted, resulting in energy differences of $\Delta E_s = \pm 50.30$ meV and ± 21.25 meV for the conduction and valence bands, respectively. These SOC-induced effects are clearly visible in the spin-resolved energy bands, where the expectation values of spins are encoded by colors (see color bars). Moreover, significant spin-splitting and unique spin-momentum locking features appear in the relativistic band structures. We recall that the non-centrosymmetric MPG of the PE phase allows both $\vec{k}/-\vec{k}$ symmetric (even-parity) and $\vec{k}/-\vec{k}$ anti-symmetric (odd-parity) bands. Due to the antiunitary $\mathcal{TM}_c$ operation, the in-plane spin components (S_x and S_y) exhibit even-parity (i.e., $E(k, S_{x,y}) = E(-k, S_{x,y})$), in agreement with the MPG analysis.[7] In contrast, the sign of the out-of-plane spin component S_z has an odd parity ($E(k, S_z) = E(-k, -S_z)$), and alternates along the reciprocal path of M–K–Γ–K$'$–M$'$. Likewise, $\mathcal{TM}_c$ symmetry enforces reciprocity of the band structure; in particular, valleys K and K$'$, which are precisely related by $\mathcal{TM}_c$, display the same band energies but with opposite spin polarization E(K, S_z) = E(K$'$, $-S_z$). Furthermore, by reversing the Néel vector L, equivalent to applying the time-reversal $\mathcal{T}$ operation, the signs of the in-plane spin components are reversed, but the S_z component remains unchanged since $\mathcal{T}$ and $\mathcal{TM}_c$ have the same effect on the odd-parity spin component (**Figure S5**).

Even though both bulk and bilayer realizations of AA'-stacked H$'$-Co_2CF_2 can be classified as AMs according to SSG symmetries, we conclude that AM behavior and non-relativistic spin-splitting can be realized only in the 3D form, whereas significant spin-splitting in the 2D case is purely driven by SOC. On the other hand, the PE-AFM phase can be classified as a type-II AM,[15] due to the lack of $\mathcal{TI}$ symmetry along with the absence of FM-like behavior as enforced by the MPG $\bar{6}'m'2$.

Compensated ferrimagnetism induced by interlayer sliding

The distinct crystallographic and spin-space symmetries of the PE and FE phases result in markedly different spin-splitting behaviors in their electronic band structures. Specifically,

the PE phase is characterized by the SSG of $P^{\bar{1}}\bar{6}^{1}m^{\bar{1}}2^{\infty m}1$, corresponding to the MSG of $P\bar{6}'m'2$, while the FE phase adopts the $P^{1}3^{1}m^{1}1^{\infty m}1$ SSG and $P3m'1$ MSG.[23] To elucidate the spin-splitting effects and functional properties, we focus on the ($+P$, $+L$) configuration for detailed analysis. In the absence of SOC, breaking the $\mathcal{M}_c$ symmetry by interlayer sliding removes the equivalency between the two oppositely oriented FM monolayers, resulting in distinct Zeeman-like effective exchange fields, arising from both the different local environment of FM monolayer and AFM interlayer interactions. Consequently, the energy bands arising from the two monolayers undergo largely opposite rigid energy shifts, leading to fully spin-polarized bands and sizeable Zeeman-like spin-splitting throughout the 2D Brillouin zone, including high-symmetry points Γ and M (see upper panel of Figure 3). Since the PE–FE transition occurs without crossing a metallic point, the net FM magnetization is zero by virtue of the Luttinger theorem,[43,44] implying that the number of spin-up and spin-down channel electrons are the same. This behavior is consistent with the classification of the system as a compensated ferrimagnet based on its SSG.[23,50] Moreover, the MSG is compatible with FM behavior, classifying the FE-AFM bilayer as a type-I altermagnet.[15] Notably, accidental crossings between spin-up and spin-down bands are observed along the K–Γ–K′ path in reciprocal space, as highlighted by the dashed rectangles in Figure 3 and **Figure S6**.

More intriguingly, SOC effects have significant modifications on the band structure. As shown in the lower panel of Figure 3 and **Figure S7**, accidental degeneracies along the K–Γ–K′ reciprocal path are removed, and each energy band is characterized by opposite spin polarizations alternately distributed along the k-path.[51] We refer to this SOC-induced phenomenon as "alternating" spin-polarized bands (see **Figure S8** for details). Including SOC in the acentric FE-AFM bilayer induces strong band non-reciprocity, particularly pronounced at the Brillouin zone edges K and K′, which are no longer related due to the broken $\mathcal{T}\mathcal{M}_c$ symmetry. This peculiar band reconstruction stems from two distinct SOC-mediated mechanisms, as described by a $\boldsymbol{k}\cdot\boldsymbol{p}$ model (see **Figure S9** and the detailed analysis in the

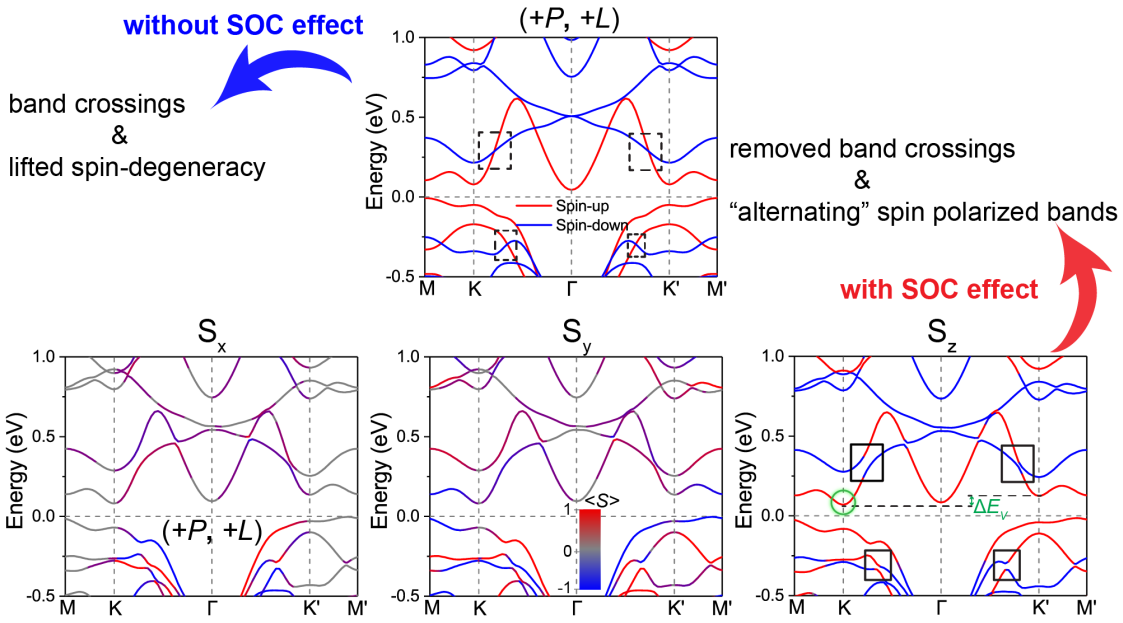

Figure 3: Calculated spin-resolved non-relativistic (upper) and relativistic (lower) band structures for the $(+P, +L)$ state of the FE H$'$-Co_2CF_2 bilayer, respectively. Band crossings along the K–Γ–K$'$ path are marked by dashed rectangles, while the removed crossings are indicated by solid rectangles. The color bar represents the expectation values of the in-plane (S_x, S_y) and out-of-plane (S_z) spin components from spin-active Co cations. Spin-valley locking at the K point is highlighted by a green circle. The Fermi level is set at 0 eV.

Supporting Information).[5] First, SOC introduces a valley-dependent correction to the Zeeman-like exchange field, rendering the K and K$'$ valleys inequivalent (i.e., non-reciprocal) with distinct spin-splitting magnitudes. Second, the polar acentric FE-AFM bilayer enables a SOC-induced Rashba coupling. This lifts spin-degenerate band crossings (indicated by solid/dashed rectangles in Figure 3, **Figure S6-S7**) and mediates in-plane band spin polarization, resulting in energy bands that exhibit alternating spin components in both magnitude and direction along the momentum axis. Along the K–Γ–K$'$ path, the in-plane spin components (S_x and S_y) exhibit alternating signs. Simultaneously, the out-of-plane spin component S_z also alternates its sign along the Γ–K and Γ–K$'$ segments of the "alternating" spin-polarized bands. As a result, the sign of "alternating" spin-polarized bands can be reversed by switching either the FE polarization P or the Néel vector L.

Tunable alternating spin-textures and MOKE response

Since the MOKE response is governed by the ferroic state (P, L), it can be tuned concurrently through FE and magnetic means. In Figure 4 (a), we present the energy profile and polarization evolution associated with the transition between the FE ($+P$, $+L$) and ($-P$, $+L$) states. Figure 4 (b) illustrates the corresponding changes in the sign of the "alternating" spin-polarized bands marked by red and blue bars. The transition from ($+P$, $+L$) to ($-P$, $+L$) is equivalent to applying the combined $\mathcal{T}\mathcal{M}_c$ symmetry operation to the ($+P$, $+L$) state (see **Figure S3**).[52] This operation simultaneously reverses both the spin-orbit and Zeeman fields, resulting in the switching of all spin components and the swapping of K and K$'$ valleys. Conversely, reversing the Néel vector L ($L \rightarrow -L$) is equivalent to applying a time-reversal operation $\mathcal{T}$, which inverts the Zeeman fields and exchanges the K and K$'$ valleys. Consequently, only the out-of-plane spin component S_z changes sign. Simultaneous switching of both P and L between ($+P$, $+L$) and ($-P$, $-L$) states corresponds to the $\mathcal{M}_c$ operation, which reverses the sign of the Rashba-like spin-orbit field. In this case, only the in-plane spin components change their signs. Interestingly, the SOC effect induces a spontaneous ferro-valley polarization, characterized by a valley splitting $\Delta E_V = \pm 49.20$ meV (marked by green circles in Figure 3 and **Figure S7**). This splitting couples to the S_z component, enabling robust spin-valley locking. Consequently, reversing the sign of S_z via either the $\mathcal{T}$ or $\mathcal{T}\mathcal{M}_c$ symmetry operation can induce a sign reversal of ΔE_V at the valleys.

The modifications in spin components following either polarization switching ($P \rightarrow -P$) or Néel vector reversal ($L \rightarrow -L$) become particularly evident in the spin-texture plots. As shown in Figure 4 (c), the spin-textures near the conduction band edges are mapped for the ($+P$, $+L$), ($+P$, $-L$), ($-P$, $+L$), and ($-P$, $-L$) states, respectively. All of these spin-texture plots exhibit three-fold rotational symmetry and Rashba-type characteristics. Consistent with the schematic diagram in Figure 4 (b), flipping L under the $\mathcal{T}$ operation preserves the orientation of in-plane spin components while the out-of-plane S_z component reverses its sign. In contrast, switching P via interlayer sliding results in the reversal of

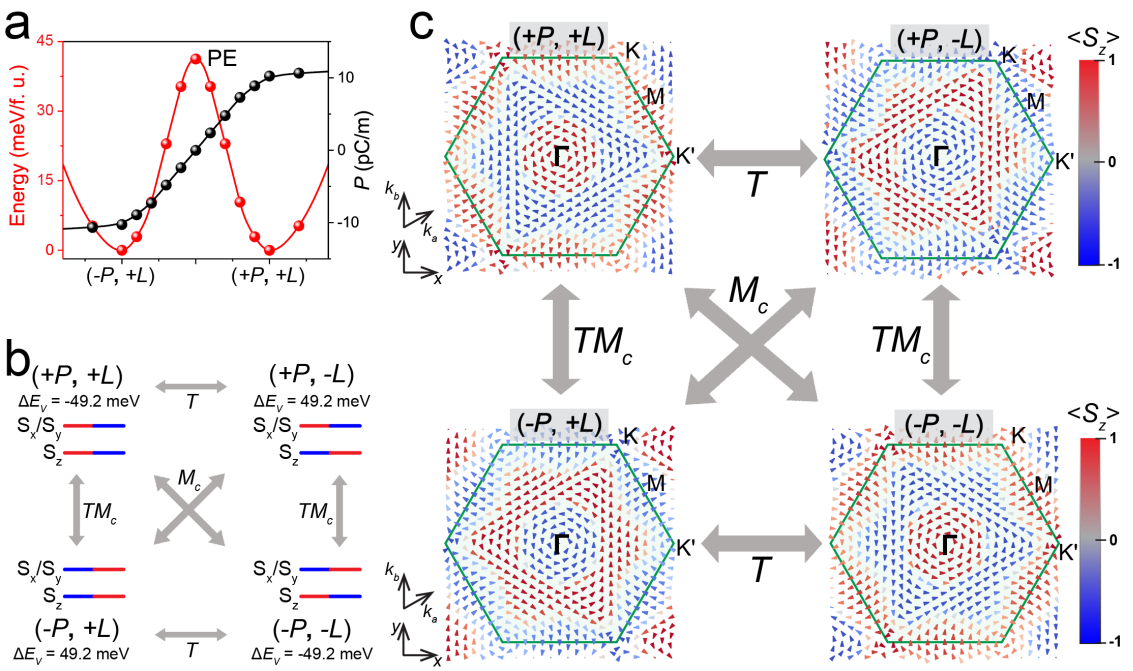

Figure 4: (a) Energy pathway (red) and evolution of out-of-plane polarization P (black) during the interlayer sliding between $\pm P$ states across the saddle point PE phase. (b) Schematic diagram illustrating the changes in the sign of spin components within the "alternating" spin-polarized bands and ferro-valley ΔE_V associated with the switching of polarization P and the flipping of Néel vector L. The alternating red and blue bars represent the signs of the S_x, S_y, and S_z spin components, respectively. (c) Calculated spin-textures around the conduction band edge of the four FE bilayers. In-plane spin components are depicted by arrows, and the color bars indicate the sign of out-of-plane spin component ($<S_z>$). The green solid lines represent the boundaries of the first Brillouin zone.

both in-plane spin components and S_z. Meanwhile, after simultaneously changing L and P, the in-plane spin orientations reverse, while the out-of-plane spin component S_z remains unchanged near the valley. Notably, the swapping of K and K$'$ points emerges when applying $\mathcal{T}$ or $\mathcal{T}\mathcal{M}_c$ operations, which is consistent with the spin-valley locking shown in Figure 3 and **Figure S7**. Similar results can also be observed in the spin-texture plots of their valence band edges, as shown in **Figure S10**.

The simultaneous breaking of $\mathcal{TI}$ and $\mathcal{T}$ symmetries of the FE bilayer is responsible for the activation of MOKE. Specifically, MOKE is closely related to the frequency (ω) dependent optical conductivity tensor (σ).[53] For 2D layered materials lacking out-of-plane periodicity, we employ a method that combines the ω-dependent effective dielectric tensor

(ε), the effective surface optical conductivity tensor $\underline{\underline{\sigma}}'$, and the effective layer thickness to simulate θ_k of the 2D FE H′-Co_2CF_2 bilayer (see the **Supporting Information** for details).[52] Figure 5 (a) shows the simulated θ_k for the 2D PE and FE bilayers. Without $\mathcal{TM}_c$-symmetry breaking, the PE phase is MOKE-inactive with $\theta_k = 0$ across the spectrum. In contrast, the MOKE becomes active in the four FE states, where the maximal θ_k magnitudes (0.37°) emerge at an incident photon energy of approximately 2.67 eV (within the visible light region). Notably, θ_k can be enhanced up to 14° by using a metamaterial substrate with refractive index $n_s = 0.78$ (**Figure S11**).[31]

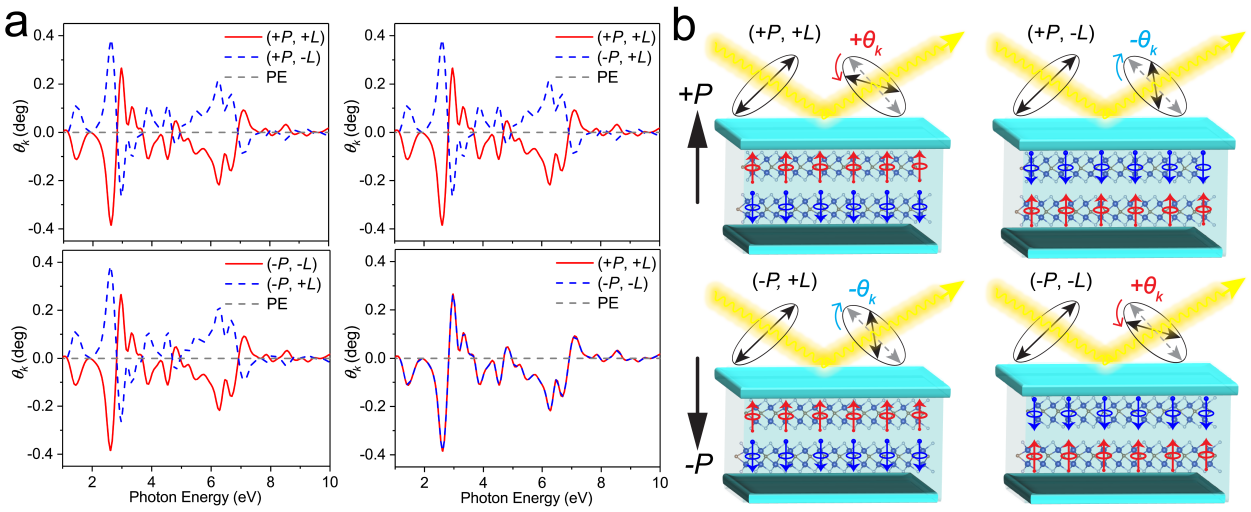

Figure 5: (a) Simulated Kerr angle θ_k as a function of incident photon energy for the PE and FE phases of H′-Co_2CF_2 bilayer. In the PE phase, MOKE is inactive with $\theta_k = 0$ over the entire photon energy range. In contrast, the maximal magnitude of θ_k occurs in the FE phase when the photon energy approaches 2.67 eV. θ_k reverses its sign after either switching P or flipping L, but remains unchanged under the simultaneous change of P and L. (b) Schematic diagram of the MOKE-based device utilizing the switching of θ_k in FE H′-Co_2CF_2 bilayer. Tuning the sign of θ_k can be achieved by interlayer sliding between $\pm P$ states or flipping the Néel vectors between $\pm L$ states. The golden wavy lines represent incident and reflected linearly polarized light. The magnetization directions of adjacent monolayers are indicated by red and blue circled arrows. The negative and positive θ_k are marked in blue and red, respectively.

Since the MOKE exhibits odd-parity under time-reversal symmetry ($\mathcal{T}$-odd), the angle θ_k will reverse its sign when $\mathcal{T}$ operation is applied. As discussed earlier, switching the polarization P or flipping the Néel vector L is equivalent to applying $\mathcal{TM}_c$ or $\mathcal{T}$ operations

on the FE H′-Co_2CF_2 bilayer, respectively.[29,52,54] Therefore, the sign of θ_k will reverse under either P–switching [$(\pm P, \pm L, \mid +\theta_k) \longrightarrow (\mp P, \pm L, \mid -\theta_k)$] or L–flipping [$(\pm P, \pm L, \mid +\theta_k) \longrightarrow (\pm P, \mp L, \mid -\theta_k)$]. In contrast, when only the operation $\mathcal{M}_c$ is applied between the $(\pm P, \pm L, \mid +\theta_k)$ and $(\mp P, \mp L, \mid +\theta_k)$ states, the sign of θ_k remains unchanged. Remarkably, the transformation rules governing MOKE are identical to those governing the S_z component in the "alternating" spin-polarized bands shown in Figure 4 (b)-(c). Hence, the spontaneous and tunable θ_k in the FE phase follows the same behavior as the "alternating" spin-polarized bands, and is sensitive to the reversal of band non-reciprocity, thus providing multiple degrees of freedom to control the electronic properties of the 2D FE H′-Co_2CF_2 bilayer.[55]

Based on the tunability of θ_k, we propose a schematic design for MOKE-active devices based on the 2D FE H′-Co_2CF_2 bilayers. As shown in Figure 5 (b), when linearly polarized light is incident on the $(+P, +L)$ state, it induces a positive Kerr rotation angle (denoted as $+\theta_k$) in the polarization plane of the reflected light. By switching the polarization direction P via an external bias or flipping the Néel vector L through current-induced spin-orbit torque,[49] the system transforms into the $(-P, +L)$ or $(+P, -L)$ state with a negative Kerr rotation $(-\theta_k)$. Above operations enable the electric or magnetic control of the logic 'ON' and 'OFF' states. Moreover, the novel dimension-dependent altermagnetism and compensated ferrimagnetism suggest that multiferroic H′-Co_2CF_2 could exhibit rich material properties and functionalities such as the anomalous Hall effect,[56] anomalous valley Hall effect,[57–59] Faraday rotation, and fully spin-polarized currents[50] in its 3D PE bulk and 2D FE bilayer structural forms, offering a platform for diverse spintronic applications.

CONCLUSIONS

In summary, combining first-principles calculations, symmetry analysis, and $\boldsymbol{k}\cdot\boldsymbol{p}$ modeling, we systematically demonstrate the tunability of unconventional magnetism and MOKE in the H′-Co_2CF_2 bilayer. The 2D non-polar PE bilayer exhibits non-relativistic spin-degenerate

bands due to the $\mathcal{M}_c$ mirror plane, while the non-relativistic spin-splitting associated with the $[\mathcal{C}_2\|\mathcal{M}_c]$ symmetry emerges in its 3D bulk phase, which indicates a dimension-driven AM crossover. Breaking the $\mathcal{M}_c$ symmetry by interlayer sliding stabilizes the FE H$'$-Co_2CF_2 bilayer with out-of-plane polarization and non-relativistic spin-splitting arising from the compensated ferrimagnetism. When SOC is included, the FE phase characterizes "alternating" spin-polarized bands due to the interplay of Zeeman and Rashba effects. By switching the orientation of sliding ferroelectricity or Néel vector, it is possible to control the ferro-valley polarization, spin-texture and θ_k simultaneously. Finally, we propose MOKE-active devices based on the 2D sliding FE H$'$-Co_2CF_2 bilayers, enabling electromagnetic control and magneto-optical detection within the visible spectrum.

COMPUTATIONAL METHODS

First-principles calculations are performed based on density functional theory (DFT) methods as implemented in the Vienna *Ab initio* Simulation Package (VASP).[60,61] We use the Perdew–Burke–Ernzerhof (PBE) exchange-correlation functional within the generalized gradient approximation (GGA).[62] A plane-wave basis set within the projector augmented wave (PAW) method[63] is employed, using a 600 eV energy cutoff. The effective Hubbard U_{eff} = 2.0 eV is applied for Co-d orbital.[40,64] The interlayer vdW interactions are simulated using DFT-D3 method developed by Grimme.[65] The crystallographic a, b and c axes refer to two in-plane and one out-of-plane (vertical) directions, respectively. 2D H$'$-Co_2CF_2 bilayers are simulated as slabs containing at least 20 Å vacuum along the c-axis. The Brillouin zones are sampled based on Monkhorst-Pack scheme[66] using 12×12×1 k-point grid. The dipole correction is included in the vacuum region.[67] The atomic positions and lattice parameters are fully optimized until the residual Hellmann-Feynman forces and stress are less than 0.001 eV/Å and 0.1 kbar, respectively. The phonon spectrum is calculated based on the finite difference method.[68] SOC effect is considered during the calculations. The vertical polarization in 2D

bilayer can be obtained from the integration of planar-averaged screening charge density.[42]

Supporting Information Available

The Supporting Information is available free of charge.

- FE polarization of H′-Co_2CF_2 monolayer, planar-averaged screening charge density of ($+P$, $+L$) state, spin densities of AFM-FE phases, relative energies of FM, AFM and NM phases, AFM configurations with $-L$ Néel vector, relativistic band structure of PE phase, non-relativistic and relativistic band structures of FE phases, the comparison of spin-degenerate, spin-splitting and "alternating" spin-polarized bands, the lower conduction bands simulated by $\boldsymbol{k}\cdot\boldsymbol{p}$ model, spin-textures around the valence band edges, the evolution of Kerr angle θ_k as a function of n_s, non-zero ξ_{xy} components of FE phases, computational details for $\boldsymbol{k}\cdot\boldsymbol{p}$ model and MOKE.

Notes

The authors declare no competing financial interest.

Acknowledgement

The authors thank Gu Mingqiang of Sun Yat-sen University for fruitful discussions. G.Y. G acknowledges the funding support from National Natural Science Foundation of China (Grant No. 11574244). N. Ding acknowledges the support from Program for Excellent Postdoctoral Talent under Grant No. 2024ZB001, and the China Postdoctoral Science Foundation under Grant No. 2024M760423. Additional funding was provided by the European Union – NextGenerationEU under the Italian MUR National Innovation Ecosystem grant ECS00000041 - VITALITY - CUP E13C22001060006. X.F. C acknowledges the support from China Scholarship Council. This work has been funded by the European Union -

NextGenerationEU, Mission 4, Component 2, under the Italian Ministry of University and Research (MUR) National Innovation Ecosystem grant ECS00000041 - VITALITY - CUP B43C22000470005. Hefei Advanced Computing Center is acknowledged for computational support.

References

(1) Zhu, Y.-P. et al. Observation of Plaid-Like Spin Splitting in a Noncoplanar Antiferromagnet. *Nature* **2024**, *626*, 523–528.

(2) Bai, L.; Feng, W.; Liu, S.; Šmejkal, L.; Mokrousov, Y.; Yao, Y. Altermagnetism: Exploring New Frontiers in Magnetism and Spintronics. *Adv. Funct. Mater.* **2024**, *34*, 2409327.

(3) Šmejkal, L.; Sinova, J.; Jungwirth, T. Emerging Research Landscape of Altermagnetism. *Phys. Rev. X* **2022**, *12*, 040501.

(4) Zhu, Y.; Chen, T.; Li, Y.; Qiao, L.; Ma, X.; Liu, C.; Hu, T.; Gao, H.; Ren, W. Multipiezo Effect in Altermagnetic V_2SeTeO Monolayer. *Nano Lett.* **2023**, *24*, 472–478.

(5) Yuan, L.-D.; Wang, Z.; Luo, J.-W.; Zunger, A. Prediction of Low-Z Collinear and Noncollinear Antiferromagnetic Compounds Having Momentum-Dependent Spin Splitting even Without Spin-Orbit Coupling. *Phys. Rev. Mater.* **2021**, *5*, 014409.

(6) Chen, X.; Liu, Y.; Liu, P.; Yu, Y.; Ren, J.; Li, J.; Zhang, A.; Liu, Q. Unconventional Magnons in Collinear Magnets Dictated by Spin Space Groups. *Nature* **2025**, *640*, 349–354.

(7) Radaelli, P. G. Tensorial Approach to Altermagnetism. *Phys. Rev. B* **2024**, *110*, 214428.

(8) Zhou, X.; Feng, W.; Zhang, R.-W.; Šmejkal, L.; Sinova, J.; Mokrousov, Y.; Yao, Y. Crystal Thermal Transport in Altermagnetic RuO_2. *Phys. Rev. Lett.* **2024**, *132*, 056701.

(9) Liu, J. et al. Absence of Altermagnetic Spin Splitting Character in Rutile Oxide RuO_2. *Phys. Rev. Lett.* **2024**, *133*, 176401.

(10) Yang, G. et al. Three-Dimensional Mapping of the Altermagnetic Spin Splitting in CrSb. *Nat. Commun.* **2025**, *16*, 1442.

(11) Reichlova, H. et al. Observation of a Spontaneous Anomalous Hall Response in the Mn_5Si_3 d-wave Altermagnet Candidate. *Nat. Commun.* **2024**, *15*, 4961.

(12) Šmejkal, L.; Sinova, J.; Jungwirth, T. Beyond Conventional Ferromagnetism and Antiferromagnetism: A Phase with Nonrelativistic Spin and Crystal Rotation Symmetry. *Phys. Rev. X* **2022**, *12*, 031042.

(13) Gu, M.; Liu, Y.; Zhu, H.; Yananose, K.; Chen, X.; Hu, Y.; Alessandro, S.; Liu, Q. Ferroelectric Switchable Altermagnetism. *Phys. Rev. Lett.* **2025**, *134*, 106802.

(14) Krempasky, J. et al. Altermagnetic Lifting of Kramers Spin Degeneracy. *Nature* **2024**, *626*, 517–522.

(15) Cheong, S.-W.; Huang, F.-T. Altermagnetism with Non-Collinear Spins. *NPJ Quantum Mater.* **2024**, *9*, 13.

(16) Šmejkal, L.; Hellenes, A. B.; Gonzalez-Hernandez, R.; Sinova, J.; Jungwirth, T. Giant and Tunneling Magnetoresistance in Unconventional Collinear Antiferromagnets with Nonrelativistic-Momentum. *Phys. Rev. X* **2022**, *12*, 011028.

(17) Bai, H.; Han, L.; Feng, X. Y.; Zhou, Y. J.; Su, R. X.; Wang, Q.; Liao, L. Y.; Zhu, W. X.; Chen, X. Z.; Pan, F.; Fan, X. L.; Song, C. Observation of Spin Splitting Torque in a Collinear Antiferromagnet RuO_2. *Phys. Rev. Lett.* **2022**, *128*, 197202.

(18) Feng, Z. et al. An Anomalous Hall Effect in Altermagnetic Ruthenium Dioxide. *Nat. Electron.* **2022**, *5*, 735–743.

(19) Zhang, R.-W.; Cui, C.; Li, R.; Duan, J.; Li, L.; Yu, Z.-M.; Yao, Y. Predictable Gate-Field Control of Spin in Altermagnets with Spin-Layer Coupling. *Phys. Rev. Lett.* **2024**, *133*, 056401.

(20) Šmejkal, L.; Marmodoro, A.; Ahn, K.-H.; González-Hernández, R.; Turek, I.; Mankovsky, S.; Ebert, H.; D′Souza, S. W.; Šipr, O.; Sinova, J.; Jungwirth, T. Chiral Magnons in Altermagnetic RuO_2. *Phys. Rev. Lett.* **2023**, *131*, 256703.

(21) Liu, Z.; Ozeki, M.; Asai, S.; Itoh, S.; Masuda, T. Chiral Split Magnon in Altermagnetic MnTe. *Phys. Rev. Lett.* **2024**, *133*, 156702.

(22) Pan, B.; Zhou, P.; Lyu, P.; Xiao, H.; Yang, X.; Sun, L. General Stacking Theory for Altermagnetism in Bilayer Systems. *Phys. Rev. Lett.* **2024**, *133*, 166701.

(23) Chen, X.; Ren, J.; Zhu, Y.; Yu, Y.; Zhang, A.; Liu, P.; Li, J.; Liu, Y.; Li, C.; Liu, Q. Enumeration and Representation Theory of Spin Space Groups. *Phys. Rev. X* **2024**, *14*, 031038.

(24) Fan, F.-R.; Wu, H.; Nabok, D.; Hu, S.; Ren, W.; Draxl, C.; Stroppa, A. Electric-Magneto-Optical Kerr Effect in a Hybrid Organic-Inorganic Perovskite. *J. Am. Chem. Soc.* **2017**, *139*, 12883–12886.

(25) Huang, F.; Kief, M. T.; Mankey, G. J.; Willis, R. F. Magnetism in the Few-Monolayers Limit: A Surface Magneto-Optic Kerr-Effect Study of the Magnetic Behavior of Ultrathin Films of Co, Ni, and Co-Ni Alloys on Cu(100) and Cu(111). *Phys. Rev. B* **1994**, *49*, 3962–3971.

(26) Feng, W.; Guo, G.-Y.; Zhou, J.; Yao, Y.; Niu, Q. Large Magneto-Optical Kerr Effect in Noncollinear Antiferromagnets Mn_3X (X = Rh, Ir, Pt). *Phys. Rev. B* **2015**, *92*, 144426.

(27) Zhou, X.; Feng, W.; Yang, X.; Guo, G.-Y.; Yao, Y. Crystal Chirality Magneto-Optical Effects in Collinear Antiferromagnets. *Phys. Rev. B* **2021**, *104*, 024401.

(28) Lee, S.; Lee, S.; Jung, S.; Jung, J.; Kim, D.; Lee, Y.; Seok, B.; Kim, J.; Park, B. G.; Šmejkal, L.; Kang, C. J.; Kim, C. Broken Kramers Degeneracy in Altermagnetic MnTe. *Phys. Rev. Lett.* **2024**, *132*, 036702.

(29) Yananose, K.; Radaelli, P. G.; Cuoco, M.; Yu, J.; Stroppa, A. Activating Magnetoelectric Optical Properties by Twisting Antiferromagnetic Bilayers. *Phys. Rev. B* **2022**, *106*, 184408.

(30) Wang, P.; Liu, Q.; Liu, N.; Kuang, M.; Yang, T.; Wang, B.; Ju, M.; Yuan, H.; Jiang, X.; Zhao, J. Electric Field-Controlled Magneto-Optical Kerr Effect in A-Type Antiferromagnetic Fe_2CX_2 (X = F, Cl) and Its Janus Monolayer. *ACS Appl. Mater. Inter.* **2023**, *15*, 52767–52775.

(31) Kinsey, N.; DeVault, C.; Boltasseva, A.; Shalaev, V. M. Near-Zero-Index Materials for Photonics. *Nat. Rev. Mater.* **2019**, *4*, 742–760.

(32) Sun, W.; Yang, C.; Wang, W.; Liu, Y.; Wang, X.; Huang, S.; Cheng, Z. Proposing Altermagnetic-Ferroelectric Type-III Multiferroics with Robust Magnetoelectric Coupling. *Adv. Mater.* **2025**, 2502575.

(33) Zhu, Z.; Duan, X.; Zhang, J.; Hao, B.; Zutic, I.; Zhou, T. Two-Dimensional Ferroelectric Altermagnets: From Model to Material Realization. *Nano Lett.* **2025**, *25*, 9456–9462.

(34) Duan, X.; Zhang, J.; Zhu, Z.; Liu, Y.; Zhang, Z.; Zutic, I.; Zhou, T. Antiferroelectric Altermagnets: Antiferroelectricity Alters Magnets. *Phys. Rev. Lett.* **2025**, *134*, 106801.

(35) Igor, M.; Rafael, G.-H.; Šmejkal, L. *Induced Monolayer Altermagnetism in $MnP(S,Se)_3$ and FeSe* 2024, arXiv:2309.02355, arXiv. https://arxiv.org/abs/2309.02355.

(36) Sivadas, N.; Okamoto, S.; Xu, X.; Fennie, C. J.; Xiao, D. Stacking-Dependent Magnetism in Bilayer CrI_3. *Nano Lett.* **2018**, *18*, 7658–7664.

(37) Chen, X.; Ding, X.; Gou, G.; Zeng, X. C. Strong Sliding Ferroelectricity and Interlayer Sliding Controllable Spintronic Effect in Two-Dimensional HgI_2 Layers. *Nano Lett.* **2024**, *24*, 3089–3096.

(38) Xun, W.; Wu, C.; Sun, H.; Zhang, W.; Wu, Y.-Z.; Li, P. Coexisting Magnetism, Ferroelectric, and Ferrovalley Multiferroic in Stacking-Dependent Two-Dimensional Materials. *Nano Lett.* **2024**, *24*, 3541–3547.

(39) Wu, C.; Sun, H.; Dong, P.; Wu, Y.-Z.; Li, P. Coexisting Triferroic and Multiple Types of Valley Polarization by Structural Phase Transition in 2D Materials. *Adv. Funct. Mater.* **2025**, *35*, 2501506.

(40) Huang, C.; Zhou, J.; Sun, H.; Wu, F.; Hou, Y.; Kan, E. Toward Room-Temperature Electrical Control of Magnetic Order in Multiferroic van der Waals Materials. *Nano Lett.* **2022**, *22*, 5191–5197.

(41) Jariwala, D.; Sangwan, V. K.; Lauhon, L. J.; Marks, T. J.; Hersam, M. C. Emerging Device Applications for Semiconducting Two-Dimensional Transition Metal Dichalcogenides. *ACS Nano* **2014**, *8*, 1102–1120.

(42) Meyer, B.; Vanderbilt, D. *Ab Initio* Study of $BaTiO_3$ and $PbTiO_3$ Surfaces in External Electric Fields. *Phys. Rev. B* **2001**, *63*, 205426.

(43) Luttinger, J. M.; Ward, J. C. Ground-State Energy of a Many-Fermion System. II. *Phys. Rev.* **1960**, *118*, 1417–1427.

(44) Luttinger, J. M. Fermi Surface and Some Simple Equilibrium Properties of a System of Interacting Fermions. *Phys. Rev.* **1960**, *119*, 1153–1163.

(45) Mazin, I. Altermagnetism-A New Punch Line of Fundamental Magnetism. *Phys. Rev. X* **2022**, *12*, 040002.

(46) Yasuda, K.; Zalys-Geller, E.; Wang, X.; Bennett, D.; Cheema, S. S.; Watanabe, K.; Taniguchi, T.; Kaxiras, E.; Jarillo-Herrero, P.; Ashoori, R. Ultrafast High-Endurance Memory based on Sliding Ferroelectrics. *Science* **2024**, *385*, 53–56.

(47) He, R.; Wang, H.; Deng, F.; Gao, Y.; Zhang, B.; Shi, Y.; Li, R.-W.; Zhong, Z. Switching Two-Dimensional Sliding Ferroelectrics by Mechanical Bending. *Phys. Rev. Lett.* **2025**, *134*, 076101.

(48) Wang, J.; Li, X.; Ma, X.; Chen, L.; Liu, J.-M.; Duan, C.-G.; Iniguez-Gonzalez, J.; Wu, D.; Yang, Y. Ultrafast Switching of Sliding Polarization and Dynamical Magnetic Field in van der Waals Bilayers Induced by Light. *Phys. Rev. Lett.* **2024**, *133*, 126801.

(49) Wadley, P. et al. Electrical Switching of an Antiferromagnet. *Science* **2016**, *351*, 587–590.

(50) Liu, Y.; Guo, S.-D.; Li, Y.; Liu, C.-C. Two-Dimensional Fully Compensated Ferrimagnetism. *Phys. Rev. Lett.* **2025**, *134*, 116703.

(51) Feng, Y.; Dai, Y.; Huang, B.; Kou, L.; Ma, Y. Layer Hall Effect in Multiferroic Two-Dimensional Materials. *Nano Lett.* **2023**, *23*, 5367–5372.

(52) Ding, N.; Yananose, K.; Rizza, C.; Fan, F.-R.; Dong, S.; Stroppa, A. Magneto-Optical Kerr Effect in Ferroelectric Antiferromagnetic Two-Dimensional Heterostructures. *ACS Appl. Mater. Inter.* **2023**, *15*, 22282–22290.

(53) Oppeneer, P. M.; Maurer, T.; Sticht, J.; Kübler, J. *Ab Initio* Calculated Magneto-Optical Kerr Effect of Ferromagnetic Metals: Fe and Ni. *Phys. Rev. B* **1992**, *45*, 10924–10933.

(54) Feng, J.; Zhou, X.; Xu, M.; Shi, J.; Li, Y. Layer Control of Magneto-Optical Effects and Their Quantization in Spin-Valley Splitting Antiferromagnets. *Nano Lett.* **2024**, *24*, 3898–3905.

(55) Sun, W.; Ye, H.; Liang, L.; Ding, N.; Dong, S.; Wang, S.-S. Stacking-Dependent Ferroicity of a Reversed Bilayer: Altermagnetism or Ferroelectricity. *Phys. Rev. B* **2024**, *110*, 224418.

(56) Bai, L.; Zhang, R.-W.; Feng, W.; Yao, Y. Anomalous Hall Effect in Type IV 2D Collinear Magnets. *Phys. Rev. Lett.* **2025**, *135*, 036702.

(57) Hu, X.; Zhao, W.; Xia, W.; Sun, H.; Wu, C.; Wu, Y.-Z.; Li, P. Valley Polarization and Anomalous Valley Hall Effect in Altermagnet Ti_2Se_2S with Multipiezo Properties. *Appl. Phys. Lett.* **2025**, *127*, 011905.

(58) Sun, H.; Dong, P.; Wu, C.; Li, P. Multifield-Induced Antiferromagnet Transformation into Altermagnet and Realized Anomalous Valley Hall Effect in Monolayer $VPSe_3$. *Phys. Rev. B* **2025**, *111*, 235431.

(59) Xun, W.; Liu, X.; Zhang, Y.; Wu, Y.-Z.; Li, P. Stacking-, Strain-Engineering Induced Altermagnetism, Multipiezo Effect, and Topological State in Two-Dimensional Materials. *Appl. Phys. Lett.* **2025**, *126*, 161903.

(60) Kresse, G.; Furthmuller, J. Efficient Iterative Schemes for *Ab Initio* Total-Energy Calculations Using a Plane-Wave Basis Set. *Phys. Rev. B* **1996**, *54*, 11169–11186.

(61) Kresse, G.; Furthmuller, J. Efficiency of *Ab-Initio* Total Energy Calculations for Metals and Semiconductors Using a Plane-Wave Basis Set. *Comp. Mater. Sci.* **1996**, *6*, 15–50.

(62) Perdew, J. P.; Burke, K.; Ernzerhof, M. Generalized Gradient Approximation Made Simple. *Phys. Rev. Lett.* **1996**, *77*, 3865–3868.

(63) Blöchl, P. E. Projector Augmented-Wave Method. *Phys. Rev. B* **1994**, *50*, 17953–17979.

(64) Dudarev, S. L.; Botton, G. A.; Savrasov, S. Y.; Humphreys, C. J.; Sutton, A. P. Electron-Energy-Loss Spectra and the Structural Stability of Nickel Oxide: An LSDA+U Study. *Phys. Rev. B* **1998**, *57*, 1505–1509.

(65) Grimme, S.; Antony, J.; Ehrlich, S.; Krieg, H. A Consistent and Accurate *Ab Initio* Parametrization of Density Functional Dispersion Correction (DFT-D) for the 94 Elements H-Pu. *J. Chem. Phys.* **2010**, *132*, 154104.

(66) Monkhorst, H. J.; Pack, J. D. Special Points for Brillouin-Zone Integrations. *Phys. Rev. B* **1976**, *13*, 5188–5192.

(67) Bengtsson, L. Dipole Correction for Surface Supercell Calculations. *Phys. Rev. B* **1999**, *59*, 12301–12304.

(68) Togo, A.; Tanaka, I. First Principles Phonon Calculations in Materials Science. *Scr. Mater.* **2015**, *108*, 1–5.

Table of Contents

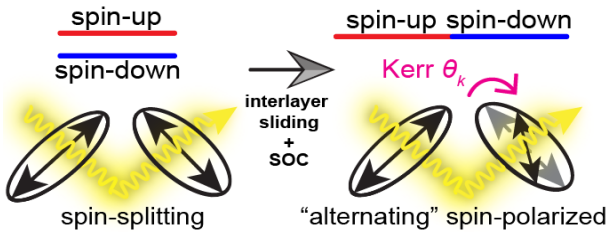

TOC

Supporting Information for Unconventional Magnetism, Sliding Ferroelectricity, and Magneto-Optical Kerr Effect in Multiferroic Bilayers

Xinfeng Chen,[†] Ning Ding,[‡] Paolo Barone,[¶] Carlo Rizza,[§] Shuai Dong,[‡] Wei Ren,[‖] Paolo G. Radaelli,[*,⊥] Gaoyang Gou,[*,†] and Alessandro Stroppa[*,#]

†*Frontier Institute of Science and Technology, State Key Laboratory of Electrical Insulation and Power Equipment, Xi'an Jiaotong University, Xi'an 710049, China.*

‡*School of Physics, Southeast University, Nanjing 211189, China.*

¶*CNR-SPIN, Area della Ricerca di Tor Vergata, Via del Fosso del Cavaliere 100, I-00133 Rome, Italy.*

§*Department of Physical and Chemical Sciences, University of L'Aquila, Via Vetoio I-67100 Coppito, L'Aquila, Italy.*

‖*Physics Department, Shanghai Key Laboratory of High Temperature Superconductors, State Key Laboratory of Advanced Special Steel, International Centre of Quantum and Molecular Structures, Shanghai University, Shanghai 200444, China.*

⊥*Clarendon Laboratory, Department of Physics, University of Oxford, Oxford OX1 3PU, United Kingdom.*

#*CNR-SPIN, c/o Department of Physical and Chemical Sciences, University of L'Aquila, Via Vetoio I-67100 Coppito, L'Aquila, Italy.*

E-mail: paolo.radaelli@physics.ox.ac.uk; gougaoyang@mail.xjtu.edu.cn; alessandro.stroppa@spin.cnr.it

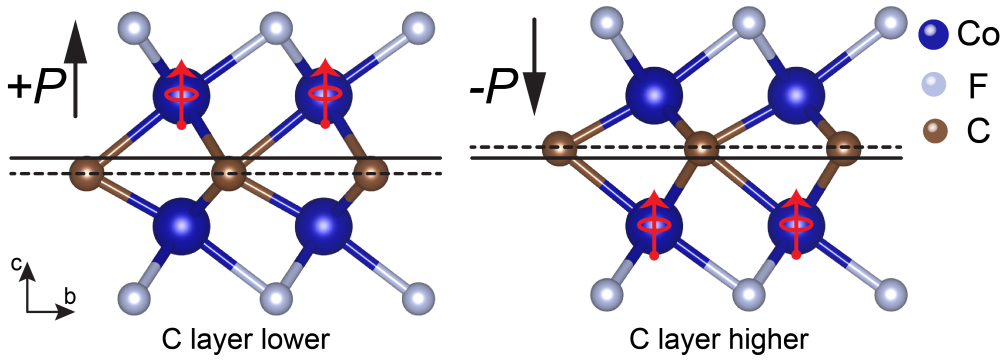

Figure S 1: Crystal structures of the H′-Co_2CF_2 monolayer with positive (left) and negative (right) FE polarization P along the out-of-plane polar axis. Due to the off-center displacement of the Co cation, the C atomic layer (marked by the dashed line) shifts away from the central atomic plane (marked by the black lines) between two adjacent Co layers, forming $\pm P$ states with FE polarization along the $\pm c$-axis.

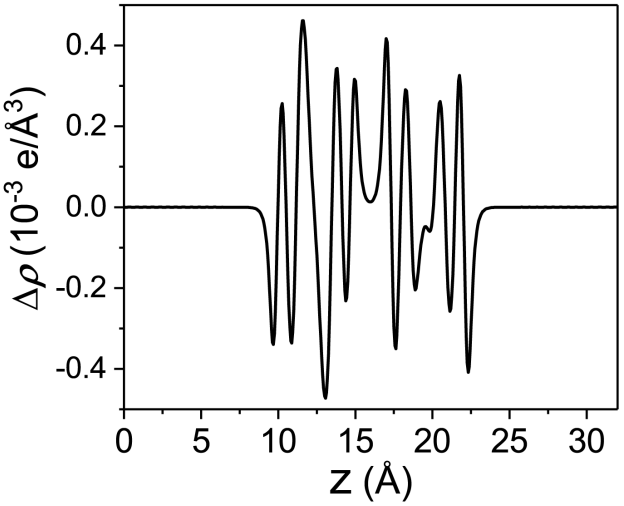

Figure S 2: Simulated planar-averaged screening charge along the out-of-plane direction for the $(+P, +L)$ state of the FE H′-Co_2CF_2 bilayer. The out-of-plane P is derived from the integration of the planar-averaged screening charge.[1]

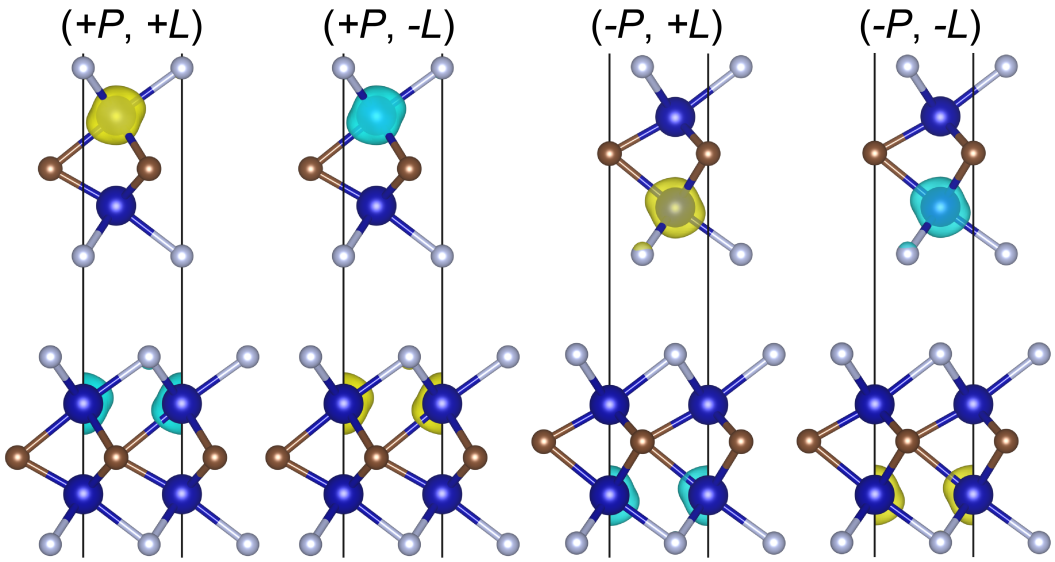

Figure S 3: Calculated spin densities for spin-active Co cations in the FE H′-Co_2CF_2 bilayer. Co, C, and F atoms are represented in blue, brown, and silver, respectively. The yellow and cyan iso-surfaces correspond to spin densities with an iso-value of $\pm$ 4.2 $\times$ 10^{-2} e/bohr^3. Magnetic moments are observed only on Co cations displaced farther away from the C atomic layer in each monolayer.

Table S 1: Simulated relative energies (meV/f.u.) for the PE and FE phases of H′-Co_2CF_2 bilayer in non-magnetic (NM), ferromagnetic (FM), and A-type antiferromagnetic (AFM) configurations. The energy of FM phase is set as the reference with zero energy.

	PE	$+P$		$-P$	
NM	627.31	616.64		622.69	
	$(+P,+L)$	$(+P,-L)$	PE	$(-P,+L)$	$(-P,-L)$
FM	0	0	62.91	0	0
A-type AFM	-0.11	-0.11	43.61	-0.11	-0.11

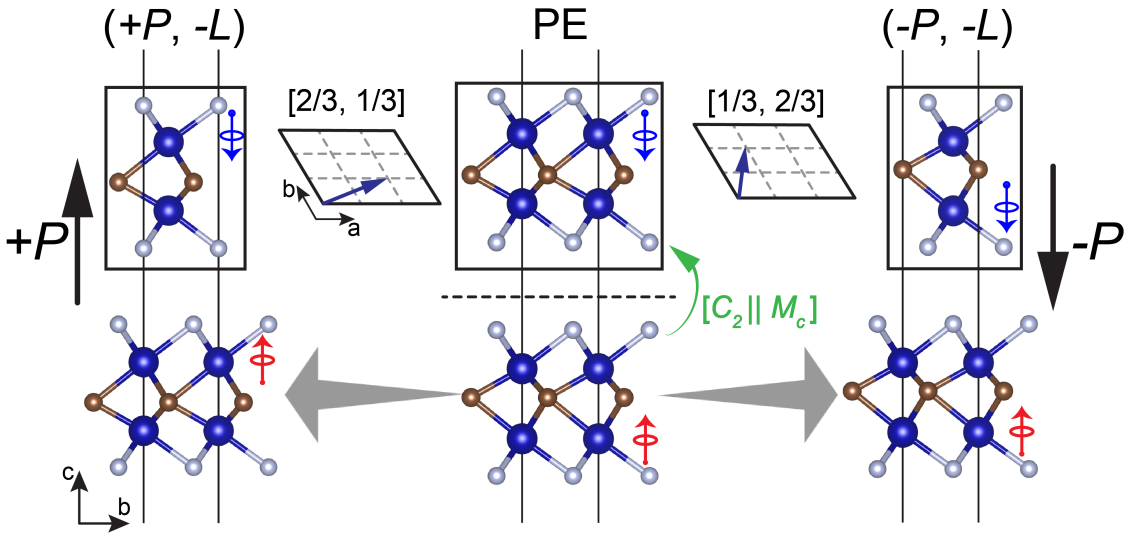

Figure S 4: Side view of the transition pathway between the PE ($P = 0$) and FE ($\pm P$) phases with the $-L$ Néel vector. The transition is achieved by the relative sliding of one monolayer towards $\boldsymbol{t} = [2/3,\ 1/3]$ or $\boldsymbol{t} = [1/3,\ 2/3]$ planar lattice vectors. The PE phase with the $-L$ Néel vector preserves the $[\mathcal{C}_2\|\mathcal{M}_c]$ spin-space symmetry.

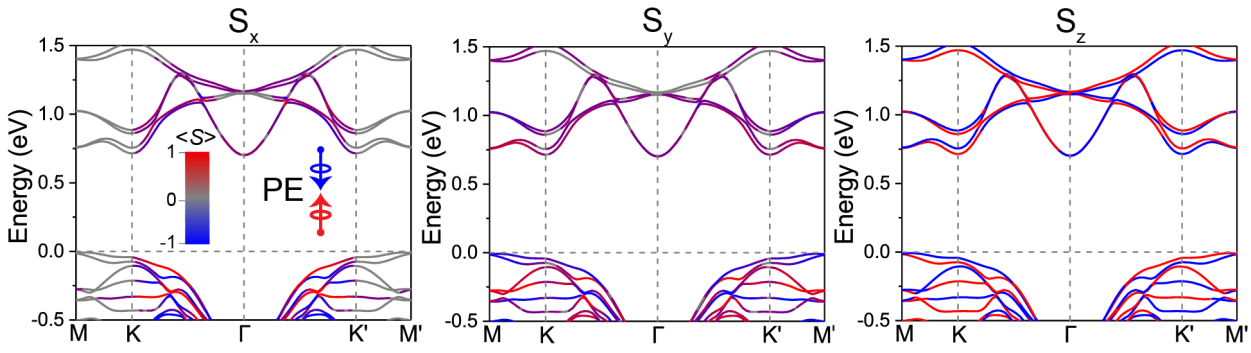

Figure S 5: Calculated relativistic spin-resolved band structures for the PE H′-Co_2CF_2 bilayer with the $-L$ Néel vector. The expectation values for in-plane spin components (S_x, S_y) and out-of-plane spin component (S_z) are represented by color bars in separate plots. The Fermi level is set at 0 eV.

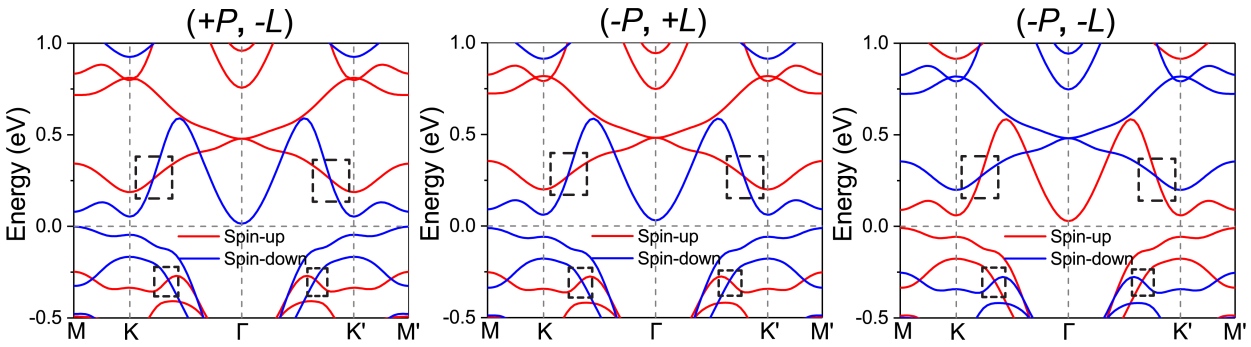

Figure S 6: Calculated non-relativistic spin-resolved band structures for the $(+P,\ -L)$, $(-P,\ +L)$, and $(-P,\ -L)$ states of the FE H$'$-Co_2CF_2 bilayer. The spin-up/spin-down band crossings along the Γ–K(K$'$) reciprocal paths are highlighted by dashed rectangles. The Fermi level is set at 0 eV.

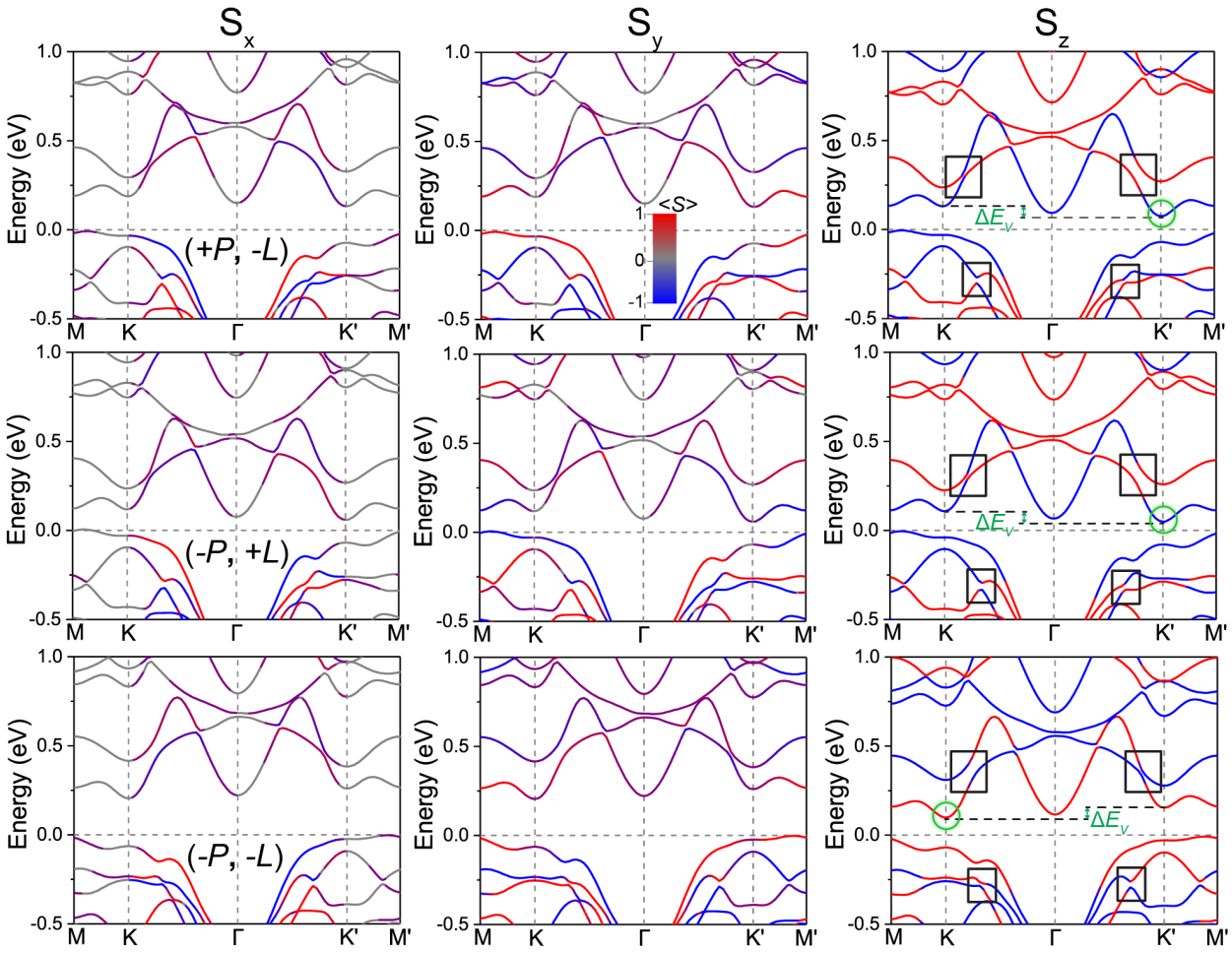

Figure S 7: Calculated relativistic spin-resolved band structures for the $(+P, -L)$, $(-P, +L)$, and $(-P, -L)$ states of the FE H′-Co_2CF_2 bilayer with SOC. The color bar indicates the expectation values of the in-plane (S_x, S_y) and out-of-plane (S_z) spin components from spin-active Co cations. The Fermi level is set at 0 eV. The removed band crossings along the K–Γ–K′ path are marked by solid rectangles. Spin-valley locking at the K(K′) points is highlighted by green circles.

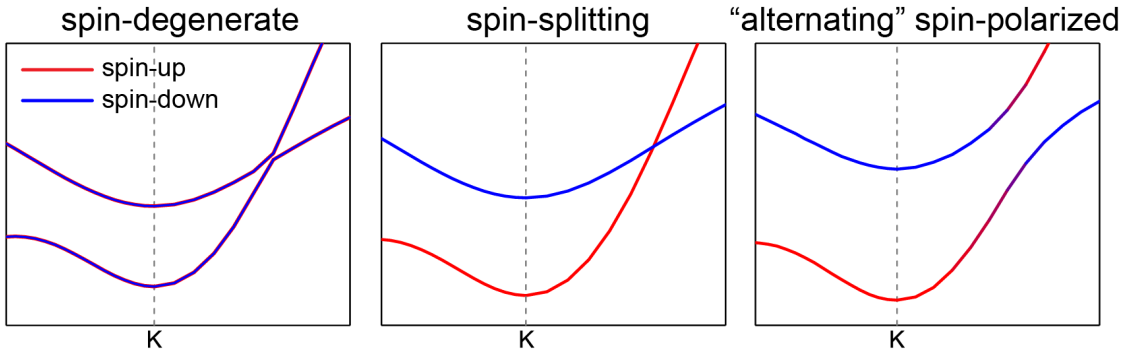

Figure S 8: The characteristics of spin-degenerate, spin-splitting, and “alternating” spin-polarized energy bands. In the spin-degenerate and spin-splitting types, spin-up and spin-down energy bands overlap and cross, respectively. In contrast, in the “alternating” spin-polarized type, opposite spin components alternate along each energy band.

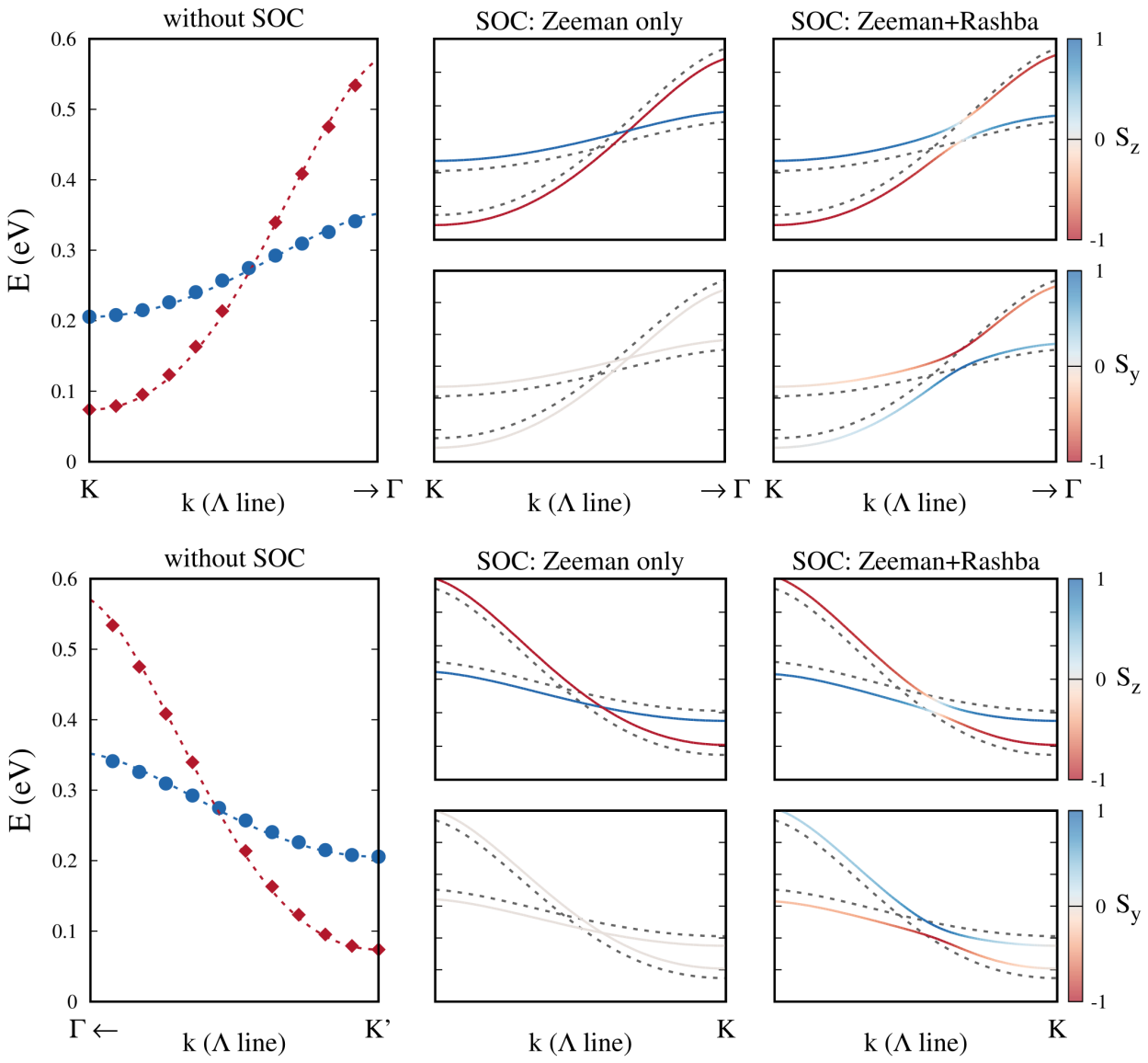

Figure S 9: The lower conduction bands along the Γ–K (top) and Γ–K′ (bottom) paths, simulated using the $\boldsymbol{k}\cdot\boldsymbol{p}$ model. Cartesian axes are taken such that the $\hat{x}$ axis is parallel to the high-symmetry line Λ (K-Γ-K′). Without SOC: The dots represent DFT results, while the lines correspond to the polynomial fit of the DFT data points. With SOC: the color maps represent the S_z (upper) and S_y (lower) spin components of the bands, while dotted lines represent band dispersion without SOC. Zeeman-only: Only the Zeeman-like correction is included, with $A_z = \mp\, 0.03$ eV; a pair of band crossings remains and shifts away from (towards) the K (K′) point. Zeeman+Rashba: With both Zeeman-like and Rashba SOC contributions included ($P_z = 0.08\ 2\pi$eV/a); the Rashba effect opens anti-crossings and induces a spin component perpendicular to the Λ line, strongly affecting S_z (bottom row).

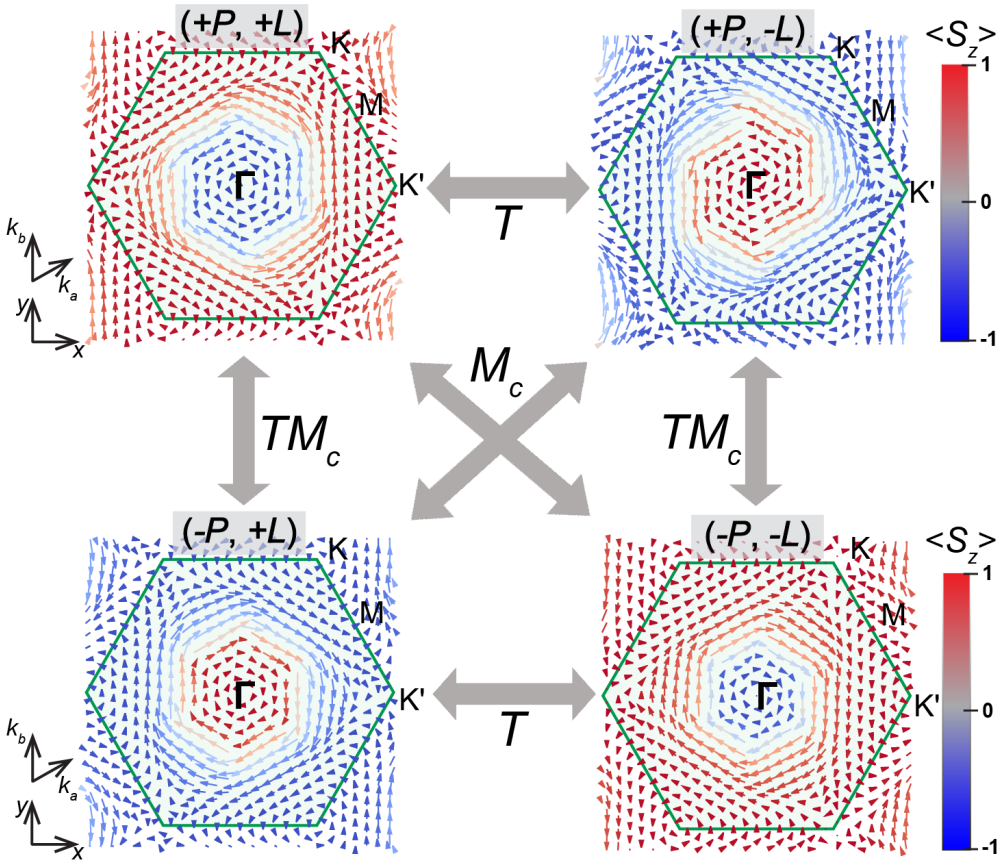

Figure S 10: Spin-texture plots of the valence band edges for the $(+P,\ +L)$, $(+P,\ -L)$, $(-P,\ +L)$, and $(-P,\ -L)$ states of the FE H′-Co_2CF_2 bilayer. In-plane spin components are represented by arrows, while the color bars indicate the sign of the out-of-plane spin component ($<S_z>$). The green solid lines represent the boundaries of the first Brillouin zone.

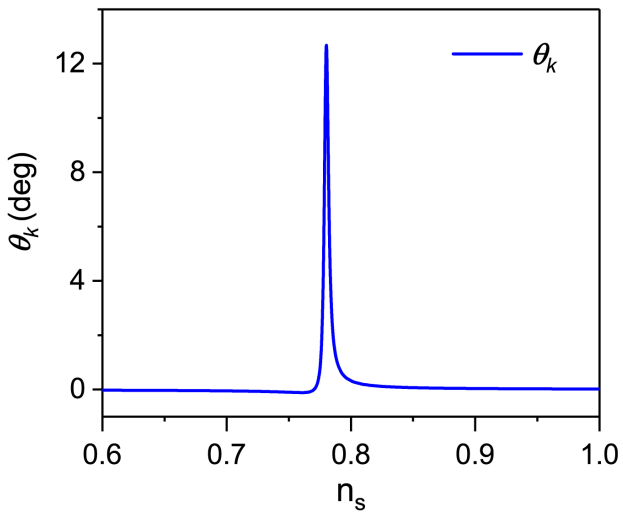

Figure S 11: The evolution of simulated Kerr angle (θ_k) as a function of the refractive index of substrate (n_s) at an incident photon energy around 2.67 eV. The θ_k magnitude peaks at 14° for $n_s \sim 0.78$.

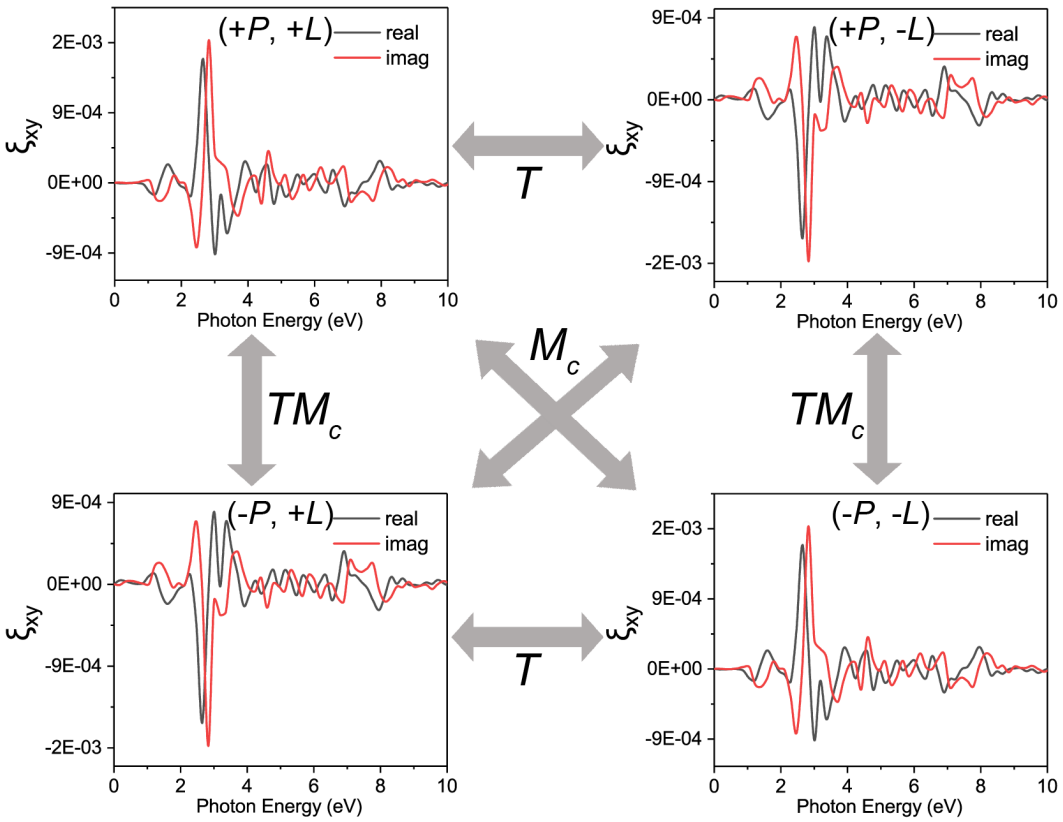

Figure S 12: Calculated non-zero ξ_{xy} components, including both the imaginary (imag) and real (real) parts, for the $(+P,\ +L)$, $(+P,\ -L)$, $(-P,\ +L)$, and $(-P,\ -L)$ states of the FE H$'$-Co_2CF_2 bilayer. The large gray arrows indicate the corresponding symmetry operations associated with P–switching or L–flipping. The sign of ξ_{xy} can be reversed under the symmetry operations of $\mathcal{T}$ or $\mathcal{T}\mathcal{M}_c$, while it remains invariant under the $\mathcal{M}_c$ operation.

Computational Details of $k \cdot p$ Model

Symmetry Analysis and Band Structure

The FE H$'$-Co_2CF_2 bilayer with AB stacking belongs to the $P3m1$ space group, which includes threefold rotations $3^{\pm}001$ along the out-of-plane c-axis and three vertical mirror planes: $\mathcal{M}_{110}$, $\mathcal{M}_{100}$, and $\mathcal{M}_{010}$. Two Co cations from each monolayer occupy the $1a$ and $1c$ Wyckoff positions in the upper and lower layers, respectively. In the PE phase, with $P\bar{6}m2$ space group, Co cations occupy the $2g$ Wyckoff position, which are related by the horizontal mirror plane $\mathcal{M}_c$ or by a π-rotation about one of the three in-plane twofold rotational axes. The AFM configuration consists of two FM layers with opposite magnetization, with the magnetic moments aligned along the perpendicular c direction. The corresponding magnetic space group (MSG) is type III, with $P3m'1$ in the FE phase and $P\bar{6}'m'2$ in the PE phase. Notably, in the FE stacking, the same magnetic symmetries are preserved for both the AFM and fully FM configurations as long as the magnetic moments are parallel to the c-axis. However, in the PE structure, different magnetic symmetries are observed for the two magnetic configurations, even when the magnetic moments are aligned along the out-of-plane direction.

In the AFM-PE structure without SOC, all bands are twofold degenerate due to the mirror plane in bilayer. The Zeeman-like band splitting occurring in a FM monolayer is mirrored in the opposite layer, but with the band spin-polarization exchanged, due to the opposite effective exchange field. This results in a hidden Zeeman-splitting effect. In the AFM-FE phase, however, there is no such compensating mechanism. Generally, each spin-splitting pair of bands from a given layer will be energy-shifted with respect to the corresponding spin-split bands from the other layer. This is consistent with the fact that both FM and AFM configurations share the same MSG.

Notably, the PE phase shows a band splitting around 120 meV at the K point (459 meV at the Γ point), comparable to the FE phase (around 131 meV at the K and 448 meV at the Γ points). While a difference is to be expected due to different interlayer interactions, the order of magnitude remains similar. Two qualitative considerations arise from these

observations:

(i) The FE phase behaves similarly to a ferromagnet, but with compensation in its insulating state. Specifically, the integral of the densities of states for spin-up and spin-down electrons up to the Fermi level are exactly equal, implying a balanced distribution of spin populations in the system;

(ii) The effects of reversing P (polarization) and L (Néel vector) can be qualitatively understood as follows. Reversing P can be viewed as swapping the positions of the layers while keeping their magnetizations fixed. In this case, the spin polarization at the band edges, which in the $+P$ configuration comes from the top layer, will be reversed in the $-P$ state, as the spin polarization now originates from the lower layer, which has the opposite magnetization. Reversing L, on the other hand, maintains the character of the layers and merely switches the order of the Zeeman-split, spin-polarized bands. This change does not affect the layer's contribution to the polarization, but it does switch the relative energy positions of the spin-split bands.

Effective Model and SOC-Induced Anticrossing of Bands

Within a one-particle approximation, the electronic properties of a magnetic system are described by a set of one-particle wave functions satisfying a self-consistent Schrödinger equation $H\Psi_{nkj} = \epsilon_{nj}(k)\Psi_{nkj}$, where the Hamiltonian can be decomposed as:

$$H = H_{kit} + H_{Har} + H_{ex} + H_{SOC} \tag{1}$$

where H_{kit} and H_{Har} correspond to the kinetic and Hartree self-consistent potential terms, respectively, and H_{SOC} represents the SOC term. H_{ex} is the self-consistent Hartree-Fock exchange term that is responsible for a Zeeman-like splitting of electronic bands for spin-up and spin-down electrons in ferromagnets. H_{kit} exhibits complete translational and rotational symmetry, while H_{Har} is invariant under all space group operations of the crystalline system under scrutiny. H_{SOC} is in general invariant under double space group operations and $\mathcal{T}$ symmetry. In contrast, the self-consistent H_{ex} in ferromagnets distinguishes between up and

down spins, thus explicitly breaking $\mathcal{T}$ symmetry, even though it does not fix the direction of spin quantization axis with respect to crystalline directions. In order to remove this ambiguity when SOC is taken into account, a common approximation for ferromagnets consists of expressing the exchange term as:

$$H_{ex} = \mathbf{B} \cdot \sigma = -\frac{1}{2} \lim_{\mathcal{B}\to 0} \frac{\Delta E}{|\mathcal{B}|} \mathcal{B} \cdot \sigma \tag{2}$$

where $\mathcal{B}$ is an auxiliary magnetic field having no other effect than fixing the spin quantization axis and ΔE is the Zeeman-like splitting between energy levels for spin-up and spin-down electrons.[2] For the FE systems, one can generalize the argument above by assuming that ΔE is a layer-dependent quantity, $\tau \Delta E$, with $\tau = \pm 1$ corresponding to the top/bottom layer. Within this approximation that fixes the spin quantization axis, the full Hamiltonian in Equation 1 and the term in Equation 2 must be invariant under all MSG operations, explicitly taking into account how $\mathcal{T}$ is broken and/or combines with $\vec{t}/\mathcal{R}$ symmetry elements. Hence, the most stringent symmetry constraints are imposed by the magnetic group operations.

One can therefore use magnetic double space group to label wavefunctions at high-symmetry points and lines, and adopt a $\boldsymbol{k}\cdot\boldsymbol{p}$ perturbation-theory approach for SOC, assuming one knows the eigensolutions of the single-particle Hamiltonian $H_0 = H_{kit} + H_{Har} + H_{ex}$. The SOC term can be decomposed into the following contributions (in atomic units) when the Hamiltonian is expanded around a given momentum k_0:

$$H_{SOC} = \frac{1}{c^2}(\nabla V \times p) \cdot \sigma + \frac{1}{c^2}(k \times \sigma) \cdot \nabla V \tag{3}$$

where V is the crystal potential and c is the velocity of light. The first term represents the SOC perturbation acting on the states at k_0, while the second term accounts for the linear-order correction in k, both explicitly depending on spin degrees of freedom. The non-zero matrix elements of SOC perturbation on a basis of unperturbed eigenfunctions can be deduced by using group-theory tools, applying the following master equation:[3]

$$\langle a\rangle_{ij}\mathbf{R} = \sum_{ll'} D_{il}(R) D^{*}_{jl'}(R) \langle a\rangle_{ll'} \tag{4}$$

where a is a vector operator, R is a symmetry element (with $\mathbf{R}$ the corresponding 3×3 transformation matrix), $\langle a\rangle_{ij} \equiv \langle \psi_i | a | \psi_j \rangle$ denotes the matrix element of the operator with respect to eigenstates labeled by their irreducible co-representation (eventually including its dimension, $i = 1...d$) and $\mathbf{D}(R)$ is the $d \times d$ representation matrix of the irreducible representation for R. Two vector operators enter in the SOC perturbation: $\nabla V \times p \equiv \mathbf{A}$, an axial vector odd under $\mathcal{T}$ reversal, and the polar vector $\nabla V \equiv \boldsymbol{P}$ that is even under $\mathcal{T}$ reversal (indeed it transforms as polarization). In addition to SOC effects, the standard $\boldsymbol{k}\cdot\boldsymbol{p}$ term needs to be considered, involving the matrix element of the operator $\boldsymbol{p}$, which is polar and odd under $\mathcal{T}$ operation.

The band co-representations for the magnetic double space group $P3m'1$ are all one-dimensional, in agreement with the fact that all bands are non-degenerate. We first focus for the sake of clarity on the pair of spin-split lowest CB along the $\Lambda \equiv$ K-Γ line, for which there exists a single irreducible co-representation for spin-1/2 states, $\bar{\Lambda}_2$. Note that this fact does not imply that all bands have the same energy: essential band degeneracies are related to the dimensionality of irreducible representations, not to the fact that bands share the same representation. All band crossing occur therefore at accidental degeneracy point. The eigenfunctions of the unperturbed Hamiltonian H_0 can be denoted as $\psi_{2\uparrow}$ and $\psi_{2\downarrow}$, with energies $\epsilon_{2\uparrow}(k) \neq \epsilon_{2\downarrow}(k)$ and k restricted along the considered high-symmetry line. The magnetic little group of line Λ comprises the unitary identity operation and the antiunitary $m'_{\perp}$ operation, a vertical reflection plane orthogonal to the high-symmetry line composed with $\mathcal{T}$ symmetry. As both bands belong to the same irreducible co-representation, the right-hand term of the master Equation 4 is trivial, and one has:

$$\langle a\rangle_{ij}\mathbf{R} = \langle a\rangle_{ij} \tag{5}$$

The left-hand term can be worked out determining how the antiunitary operation $m'_{\perp}$ acts

on the three vector operators $\mathbf{A}$, ∇V, and $\boldsymbol{p}$. Taking $\hat{x}$ as the direction of the high-symmetry line, one has:

$$\langle \boldsymbol{A} \rangle_{ij} \mathbf{R} = (-A_x, A_y, A_z) \tag{6}$$

$$\langle \boldsymbol{P} \rangle_{ij} \mathbf{R} = (-P_x, P_y, P_z) \tag{7}$$

$$\langle \boldsymbol{p} \rangle_{ij} \mathbf{R} = (p_x, -p_y, -p_z) \tag{8}$$

implying that the only matrix elements allowed by magnetic symmetries along the Λ line are $\langle A_y \rangle_{ij}$, $\langle A_z \rangle_{ij}$, $\langle P_y \rangle_{ij}$, $\langle P_z \rangle_{ij}$ and $\langle p_x \rangle_{ij}$. The lowest-order effective Hamiltonian including SOC at any crossing degeneracy point k_0, such that $\epsilon_{2\uparrow}(k_0) = \epsilon_{2\downarrow}(k_0)$ along the Λ line can be written as:

$$H(k_0) = \epsilon_2(k_0)\sigma_0 + A_z\sigma_z + A_y\sigma_y \tag{9}$$

Apparently both SOC-induced terms cause a removal of the degeneracy. However, the Zeeman-like term simply shifts the crossing point to a different point along the line, and the degeneracy is actually removed by the last term, which also causes a mixing of pure spin states leading to an additional spin-polarization $\langle \sigma_y \rangle \neq 0$ in the direction orthogonal to the high-symmetry line.

We then derive an effective $\boldsymbol{k}\cdot\boldsymbol{p}$ model around the K and K$'$ points for the lowest conduction pair of spin-split bands. The little group of K includes the unitary operations E, $3^{\pm}_{001}$ and three antiunitary operations $\mathcal{M}'_{110}$, $\mathcal{M}'_{100}$ and $\mathcal{M}'_{010}$, with three one-dimensional irreducible co-representations for half-integer spin $\bar{K}_4$, $\bar{K}_5$ and $\bar{K}_6$. One of the three vertical reflection plane is orthogonal to the K–Γ line, taken here again as parallel to the $\hat{x}$-axis, the other two being rotated by $2\pi/3$ around the out-of-plane c-axis. Notice that the points K and K$'$ are inequivalent for the considered MSG, since there is no magnetic symmetry operation of the group transforming one into the other (they are related by $\mathcal{T}$ or a vertical $\mathcal{M}$ reflection, neither of which is a symmetry element of the magnetic group). Since they do

not belong to the same star, there will be no states at K with the same energy of states at K$^{'}$ when SOC is included. This is different from the PE phase, where the twofold in-plane rotation axes make K and K$^{'}$ belong to the same star in the MSG of $P\bar{6}^{'}m^{'}2$: even when SOC is included, symmetries will impose that $\epsilon_{n\uparrow}(K) = \epsilon_{n\downarrow}(K^{'})$.

Assuming that the pair of spin-split band belongs to two copies of the same irreducible representation, the master equation for the matrix elements will have the same form of Equation 5. The presence of three-fold rotation and slanted reflection planes now introduce additional constraints, implying $\langle A_y \rangle_{ij} = 0$, $\langle P_y \rangle_{ij} = 0$ and $\langle p_x \rangle_{ij} = 0$, and leaving only the non-zero matrix elements $\langle A_z \rangle_{ij}$, $\langle P_z \rangle_{ij}$. The absence of linear-in-k correction to the non-relativistic Hamiltonian ($\langle \boldsymbol{p} \rangle_{ij} = 0$) implies that dispersion of bands around the K point will be quadratic. On the other hand, the SOC-induced correction to the lowest order in k leads the following effective model in the $(\uparrow, \downarrow)$ basis:

$$H_K(k) = H_K^0(k) + A_z\sigma_z + P_z(k_x\sigma_y - k_y\sigma_x) \tag{10}$$

where $H_K^0(k)$ is a diagonal 2×2 matrix with diagonal elements $\epsilon_\uparrow(K) \neq \epsilon_\downarrow(K)$ (eigenvalues of the non-relativistic H_0 Hamiltonian). The first SOC term is a correction to the Zeeman splitting induced by the exchange term, whereas the second term describes a Rashba coupling. The model of Equation 10 describes equally well the pairs of Zeeman-splitting arising from the top or bottom layer, that will only differ in the energy hierarchy of spin-splitting bands due to opposite layer-dependent Zeeman splitting. Similarly, the Hamiltonian describes the effect of SOC on bands around the K$^{'}$ upon a change of the sign of A_z. Eigenvalues of the model reads:

$$\epsilon_\pm(k) = \frac{1}{2}[\epsilon_\uparrow(k) + \epsilon_\downarrow(k)] \pm \frac{1}{2}\sqrt{[\epsilon_\uparrow(k) - \epsilon_\downarrow(k) + 2A_z]^2 + 4P_z^2(k_x^2 + k_y^2)} \tag{11}$$

while the Rashba interaction provides the characteristic spin-texture tangential to momentum k (valid close to the K point as considered only linear-in-k correction) with spin polarization given by:

$$\langle \sigma_x \rangle_\pm = \pm \frac{2P_z k_y}{N} \tag{12}$$

$$\langle \sigma_y \rangle_\pm = \pm \frac{2P_z k_x}{N} \tag{13}$$

where

$$N = \epsilon_+(K) - \epsilon_-(K) \equiv \sqrt{[\epsilon_\uparrow(K) - \epsilon_\downarrow(K) + 2A_z]^2 + 4P_z^2(k_x^2 + k_y^2)} \tag{14}$$

Also the z-component of spin will be affected, being $\langle \sigma_z \rangle_\pm = \pm(\epsilon_\uparrow(K) - \epsilon_\downarrow(K) + 2A_z)/N$. Notice that the Rashba coupling around the K shares the same form of the symmetry-allowed SOC term causing the anticrossing along the high-symmetry line. As anticipated, the effect of the SOC correction to Zeeman field is to shift the crossing point along the Λ line closer or farther to the K point, depending on its sign with respect to the exchange-induced Zeeman field. The anti-crossing effect is instead mediated by the SOC Rashba coupling, being larger or smaller depending on the distance from the K point, as the anticrossing splitting will be proportional to $P_z k$. However, an additional trigonal warping effect[4] is not to be excluded, given the low symmetry of the system, which might contribute to the different strength of Rashba SOC and its dependence on the distance from the high-symmetry points.

Note that the little group at the Γ point is the same as at the K and K$'$ points, even though the Zeeman splitting at Γ ($\sim$ 448 meV) is larger. Hence in-plane spin-polarization effects are expected to be smaller but still displaying a Rashba-like texture. Analogously, the high-symmetry line Λ and the high-symmetry point M share the same little group. It follows that energy bands can display a spin polarization along the c-axis (consistent with the direction of the Néel vector L) as well as a component along the M–Γ line, that is contained in the vertical reflection plane.

Computational Details of MOKE

For 2D H$'$-Co_2CF_2 bilayers without out-of-plane periodicity, we first calculate the frequency (ω)-dependent dielectric function. However, since the dielectric function is related to the cell

volume, which has uncertainty due to the artificial vacuum thickness, we define the effective dielectric function (ε) in our calculations as follows:[5,6]

$$\varepsilon_{xx} = 1 + \frac{l}{d}(\epsilon^{'}_{xx} - 1) \tag{15}$$

and

$$\varepsilon_{xy} = \frac{l}{d}\epsilon^{'}_{xy} \tag{16}$$

where l is the total thickness of our constructed model containing vacuum in units of Å, d is the thickness of the H$^{'}$-Co_2CF_2 bilayer in units of Å, $\epsilon^{'}_{xx}$ and $\epsilon^{'}_{xy}$ are the initially obtained dielectric functions calculated with vacuum. As a consequence, the redefined ω-dependent effective dielectric functions ε_{xx} and ε_{xy} are independent of the vacuum thickness. In order to calculate the MOKE in 2D materials with finite thickness, we suppose a monochromatic wave impinges at normal incidence on the 2D material. The electric field can be written as $\mathbf{E} = Re[\mathbf{E}_\omega(z)e^{-i\omega t}]$, where $\mathbf{E}_\omega(z) = E_{\omega,x}(z)\hat{\mathbf{e}}_x + E_{\omega,y}(z)\hat{\mathbf{e}}_y$ ($\hat{\mathbf{e}}_\alpha$ is an α-directed unit vector). Assuming the H$^{'}$-Co_2CF_2 bilayer lies at $z = 0$ and is much thinner than the wavelength, the electromagnetic response is determined by the optically induced surface current density $\zeta = \underline{\underline{\sigma}}^{'}\ \mathbf{E}_\omega$, where $\underline{\underline{\sigma}}^{'}$ is the surface conductivity tensor (second-rank).[7] Moreover, in the optical-electromagnetic response of 2D materials, the relation between effective dielectric function ε and effective surface optical conductivity tensor $\underline{\underline{\sigma}}^{'}$ can be written as:[8]

$$\sigma^{'}_{jp} = -id\epsilon_0\omega[(\epsilon_{jp} - 1)\delta_{jp} + \epsilon_{jp}(1 - \delta_{jp})] \tag{17}$$

where $j,\ p = x,\ y$, d is the thickness of 2D materials, δ_{jp} is the Kronecker delta, ϵ_0 is the vacuum permittivity, respectively. For an incident plane wave, we obtain the rigorous reflection coefficients by solving Maxwell equations and imposing the sheet transition condition at $z = 0$,

$$\begin{aligned}\mathbf{E}_\omega(z=0^+)-\mathbf{E}_\omega(z=0^-)=0,\\ \hat{\mathbf{e}}_z\times[\mathbf{H}_\omega(z=0^+)-\mathbf{H}_\omega(z=0^-)]=\mathbf{K},\end{aligned}\tag{18}$$

where $\mathbf{H}_\omega$ is the magnetic field. The reflection matrix connecting the amplitude of the incident ($\mathbf{E}^i_\omega$) and reflected ($\mathbf{E}^r_\omega$) electric fields is given by:

$$\begin{pmatrix}E^r_{\omega,x}\\ E^r_{\omega,y}\end{pmatrix}=\begin{pmatrix}r_{xx} & r_{xy}\\ r_{yx} & r_{yy}\end{pmatrix}\begin{pmatrix}E^i_{\omega,x}\\ E^i_{\omega,y}\end{pmatrix}\tag{19}$$

where

$$\begin{aligned}r_{xx}=r_{yy}=\frac{1-(\xi_{xx}+n_s)^2-\xi^2_{xy}}{(n_s+1+\xi_{xx})^2+\xi^2_{xy}},\\ r_{yx}=-r_{xy}=\frac{2\xi_{xy}}{(n_s+1+\xi_{xx})^2+\xi^2_{xy}},\end{aligned}\tag{20}$$

n_s is the refractive index of the substrate (defaulted as 1) where the 2D material lies, $\xi_{ij}=\sigma^{'}_{ij}\cdot Z_0$ $(i,j=x,y)$ is the dimensionless optical conductivity, Z_0 is the vacuum impedance. As a result, the complex Kerr angle $\phi_k=\theta_k+i\eta_k$ can be obtained as[9]

$$\phi_k=\frac{r_{yx}}{r_{xx}}=\frac{2\xi_{xy}}{1-(\xi_{xx}+n_s)^2-\xi^2_{xy}}\tag{21}$$

where η_k is the Kerr ellipticity. A crucial requirement for MOKE is the non-zero $\underline{\underline{\sigma}}^{'}$ component. Based on magnetic symmetry restrictions, PE and FE phases of the H$^{'}$-Co_2CF_2 bilayer are under the $\bar{6}^{'}m^{'}2$ and $3m^{'}$ magnetic point groups (MPGs), respectively. The second-rank $\underline{\underline{\sigma}}^{'}$ of the PE phase adopts the following form:[10]

$$\underline{\underline{\sigma}}^{'}=\begin{pmatrix}\sigma^{'}_{xx} & 0\\ 0 & \sigma^{'}_{xx}\end{pmatrix}$$

Clearly, MOKE is inactive in the PE phase. By contrast, the FE phase has $\underline{\underline{\sigma}}^{'}$ of the form:

$$\underline{\underline{\sigma}}^{'}=\begin{pmatrix}\sigma^{'}_{xx} & \sigma^{'}_{xy}\\ -\sigma^{'}_{xy} & \sigma^{'}_{xx}\end{pmatrix}$$

Obviously, spontaneous MOKE can be expected in the AFM-FE phases with "alternating" spin-polarized bands, whose non-zero ξ_{xy} components are displayed in **Figure S12**.

The Trilinear Coupling among P, L, and M_{eff}

The switching rules of the Kerr rotation θ_k discussed in this paper can be rationalized in the following trilinear coupling mechanism, due to the fully compensated ferrimagnetic (cFiM) character of the system. Besides the physical variables of P and L, we introduce an effective magneto-optical axial vector M_{eff} that captures the $\mathcal{T}$-odd sign of the antisymmetric optical response generated by the cFiM sublattices. In our case, M_{eff} is proportional to S_z (i.e., $M_{eff} \propto S_z$). Since θ_k is $\mathcal{T}$-odd, to lowest order, $\theta_k \propto M_{eff} \propto S_z$. Therefore, the sign of θ_k (sign$[\theta_k]$) is under the trilinear coupling among P, L, and M_{eff}:

$$\text{sign}[\theta_k] = \text{sign}[P \cdot L \cdot M_{eff}] \tag{22}$$

From this relation, it follows that $M_{eff} \propto P \cdot L$, i.e., $M_{eff} = \beta \cdot P \cdot L$, where $\beta > 0$. This interpretation suggests that the larger M_{eff} is, the larger the spin-split between band-pairs for a given k-point is. Therefore, it should be possible to define $M_{eff} = M_{eff}(k)$ through appropriate integration over the Brillouin zone, or equivalently, it would be possible to define $B_{eff} = B_{eff}(k)$ via S_z.

The following results in **Tables S2** are in agreement with the switching rules discussed in the main text. For fixed photon energy within the active window, the corresponding sign rules are:

$$(+P, +L) \rightarrow \text{sign}[\theta_k] = +M_{eff} \propto S_z \tag{23}$$

$$(-P, +L) \rightarrow \text{sign}[\theta_k] = -M_{eff} \propto S_z \tag{24}$$

$$(+P, -L) \rightarrow \text{sign}[\theta_k] = -M_{eff} \propto S_z \tag{25}$$

$$(-P, -L) \rightarrow \text{sign}[\theta_k] = +M_{eff} \propto S_z \tag{26}$$

Table S 2: The signs of all variables and θ_k, where the sign of θ_k is under the manipulation of P, L, and M_{eff}.

P	L	M_{eff}	θ_k
+	+	+	+
+	-	-	-
-	+	-	-
-	-	+	+

References

(1) Meyer, B.; Vanderbilt, D. *Ab Initio* Study of $BaTiO_3$ and $PbTiO_3$ Surfaces in External Electric Fields. *Phys. Rev. B* **2001**, *63*, 205426.

(2) Falicov, L. M.; Ruvalds, J. Symmetry of Wave Functions in Band Theory of Ferromagnetic Metals. *Phys. Rev.* **1968**, *172*, 498–507.

(3) Oguchi, T.; Shishidou, T. The Surface Rashba Effect: A $k \cdot p$ Perturbation Approach. *J. Phys.: Condens. Matter* **2009**, *21*, 092001.

(4) Fu, L. Hexagonal Warping Effects in the Surface States of the Topological Insulator Bi_2Te_3. *Phys. Rev. Lett.* **2009**, *103*, 266801.

(5) Gajdos, M.; Hummer, K.; Kresse, G.; Furthmuller, J.; Bechstedt, F. Linear Optical Properties in the Projector-Augmented Wave Methodology. *Phys. Rev. B* **2006**, *73*, 045112.

(6) Wu, M.; Li, Z.; Cao, T.; Louie, S. G. Physical Origin of Giant Excitonic and Magneto-Optical Responses in Two-Dimensional Ferromagnetic Insulators. *Nat. Commun.* **2019**, *10*, 2371.

(7) Yoshino, T. Theory for Oblique-Incidence Magneto-Optical Faraday and Kerr Effects in Interfaced Monolayer Graphene and Their Characteristic Features. *J. Opt. Soc. Am. B* **2013**, *30*, 1085–1091.

(8) Othman, M. A. K.; Guclu, C.; Capolino, F. Graphene-Based Tunable Hyperbolic Metamaterials and Enhanced Near-Field Absorption. *Opt. Express* **2013**, *21*, 7614–7632.

(9) Ricci, F.; D'Orazio, F.; Continenza, A.; Lucari, F.; Freeman, A. J. First-Principles Modeling of the Magneto-Optical Response in Inhomogeneous Systems. *Phys. Rev. B* **2008**, *78*, 134411.

(10) Yang, K.; Hu, W.; Wu, H.; Whangbo, M.-H.; Radaelli, P. G.; Stroppa, A. Magneto-Optical Kerr Switching Properties of $(CrI_3)_2$ and $(CrBr_3/CrI_3)$ Bilayers. *ACS Appl. Electron. Mater.* **2020**, *2*, 1373–1380.